Rochester Institute of Technology

RIT Digital Institutional Repository

Theses

8-2022

Hyper-Sensitive MEMS Pressure Sensor Array for Microscale Bubble Pressure Measurement

Yash Rajan Rasaikar
yr1598@rit.edu

Follow this and additional works at: https://repository.rit.edu/theses

Recommended Citation

Rasaikar, Yash Rajan, "Hyper-Sensitive MEMS Pressure Sensor Array for Microscale Bubble Pressure Measurement" (2022). Thesis. Rochester Institute of Technology. Accessed from

This Thesis is brought to you for free and open access by the RIT Libraries. For more information, please contact repository@rit.edu.

RIT

Hyper-Sensitive MEMS Pressure Sensor Array for Microscale Bubble Pressure Measurement

by

Yash Rajan Rasaikar

Advisor: Dr. Ivan Puchades

Thesis Submitted in Partial Fulfillment of the Requirements for the Degree of

MASTER OF SCIENCE IN ELECTRICAL ENGINEERING

Department of Electrical and Microelectronic Engineering

Kate Gleason College of Engineering

ROCHESTER INSTITUTE OF TECHNOLOGY

Rochester, New York

August 2022

Hyper-Sensitive MEMS Pressure Sensor Array for Microscale Bubble Pressure Measurement

By: Yash R. Rasaikar

Approved by:

Dr. Ivan Puchades Date
Thesis Advisor

Dr. Satish Kandlikar Date
Thesis Committee Member

Dr. Robert Pearson Date
Thesis Committee Member

Dr. Karl Hirschman Date
Thesis Committee Member

Dr. Ferat Sahin Date
Department Head

Abstract

As technology is advancing, more complex, efficient, and powerful devices are being made. These powerful devices generate a lot of heat which needs to be taken out to maximize their performance. Hence, efforts are being made to improve cooling techniques for these devices. Boiling is one such technique used in the cooling of devices. The heat transfer performance in the flow boiling systems is higher than that in pool boiling systems. With a simple add-on tapered manifold over a plain surface, we can convert pool boiling to flow boiling. This study will lead to improved performance and reliability of microelectronic devices, supercomputers, server chips, etc.

The forces from bubbles growing can provide a pumpless, self-sustained unidirectional flow effectively transforming pool boiling into the extremely efficient flow boiling, resulting in energy savings. MEMS pressure sensor array will be mounted at the end of tapered manifold to map the pressure field around a nucleating bubble. The thesis describes the design, fabrication, packaging, and testing of a bulk micromachined sensor array that is capable of monitoring the pressure progression of a bubble. The sensor utilizes an extremely thin 225 nm square Si_3N_4 diaphragm which is produced by etching away the bulk silicon with XeF_2 through holes present in the diaphragm. A unique process flow was developed to achieve the diaphragm thickness in nanometers. Four polysilicon piezoresistors, mounted on the surface of the diaphragm, where the stress is maximum, are used by the sensor.

The thesis also discusses the results obtained from the response of the fabricated sensor. Various attempts were made to get a voltage output in response to applied pressure. These values were acquired over a number of experiments repeated at similar experimental conditions to demonstrate the repeatability of the calibration data. The value of sensitivity, as derived from the slope of the linear calibration plot of Vout (V) vs Pressure (Pa) is 5.26 μV/Pa which is very close to the required target hyper-sensitivity of 5 μV/Pa.

Acknowledgment

I would like to express my sincere thanks to Dr. Ivan Puchades for providing the opportunity to research this unexplored field of engineering. His continuous support, guidance, and motivation have helped me learn about the theory of the subject and understand the details of the topic.

Besides my advisor, I would like to thank my committee members, Dr. Satish Kandlikar, Dr. Robert Pearson, and Dr. Karl Hirschman for their valuable input and productive feedback as they guided me throughout the project. I sincerely appreciate their effort to review and scrutinize my research.

I would like to thank Dr. Jayanti Venkataraman and Patricia Vicari, and everyone in the EE office for their continuous support and guidance. I would also like to thank the SMFL staff, Scott Blondell, Sean O'Brien, John Nash, Bruce Tollesen, Rich Battaglia, and Thomas Grimsley for their help and guidance in fabricating the chips and setup.

Moreover, I would like to thank William Huang, Chris Biancone, Maharshi Shukla, Connor Levine, Adheesh Ankolekar and all the members of the SMFL and TAMFL for helping me cope with the various experimental procedures and laboratory instruments. Their constant guidance has helped me throughout to troubleshoot and understand the issues I faced. Finally, I would like to thank my family for their constant support throughout the thesis. They have always encouraged me to pursue my interests.

Contents

Abstract i

Acknowledgment ii

Contents iii

List of Figures v

List of Tables viii

1.0 Introduction 1

1.1 Boiling Fundamentals 1

1.2 Conversion of Pool boiling to Flow boiling 3

1.3 MEMS Piezoresistive Pressure Sensors 4

2.0 Literature review 6

2.1 Piezoresistive Effect 6

2.2 Wheatstone Bridge 9

2.3 Design Optimization using Taguchi Approach 15

3.0 Objectives & Calculations 17

4.0 Bulk Micromachining Process 21

4.1 Gen1 Lot1 Devices 21

4.1.1 Initial Sensor Design 21

4.1.2 Fabrication G1L1 22

4.1.3 Preliminary Testing 26

4.2 Gen1 Lot2 Devices 28

4.2.1 Optimization of Array Design 28

4.2.3 Fabrication G1L2 30

4.2.2 Preliminary Testing 31

5.0 Results 34

5.1 Resistance Testing 34

5.2 Voltage testing before XeF_2 etch 35

5.3 Voltage testing after XeF_2 etch 36

6.0 Packaging 47

6.1 PCB Design 47

6.2 PCB Mask Layout 48

6.3 PCB Fabrication at SMFL 49

6.4 Final Packaged Sensors 50

7.0 Setup Schematic 53

7.1 Bubble Air-Injection Setup **53**
7.2 Experimental Setup **54**
8.0 Conclusion **56**
9.0 Future Work **57**
9.1 Proposed Surface Micromachining Process flow **58**
References **60**
Appendix **62**

List of Figures

Figure 1. Pool boiling phases 2

Figure 2. Schematic of proposed experimental setup for studying bubble squeezing mechanism in tapered micro-gap by Kandlikar et al. [17] 3

Figure 3. MEMS Pressure Sensor model adapted from [4] 4

Figure 4. Areas of maximum stress on square diaphragm 8

Figure 5. Schematic of piezoresistors in Wheatstone bridge configuration 9

Figure 6. Design of Wheatstone bridge circuit 10

Figure 7. Applying KCL to the Wheatstone bridge 11

Figure 8. Solidworks simulation of square diaphragm of L=200μm and H=1μm 13

Figure 9. The placements of 0-turn, 1-turn 15

Figure 10. Meander shaped piezoresistors. 0-turn, 1-turn and 3-turns [14] 16

Figure 11. Proposed bubble squeezing mechanism by Kandlikar et al. [17] 17

Figure 12. Schematic of a bubble in water 18

Figure 13. Maximum predicted stress at diaphragm edge vs. size of diaphragm 20

Figure 14. G1L1 pressure sensor layout 21

Figure 15. (a) Sensor array layout, (b) Mask layout of single die 22

Figure 16. Grow dry oxide on (100) Si wafers 23

Figure 17. LPCVD Polysilicon 23

Figure 18. Polysilicon doping, patterning and LPCVD Nitride 23

Figure 19. Contact cuts etch on Nitride 24

Figure 20. Aluminum sputter deposition 24

Figure 21. Aluminum wet etch 24

Figure 22. Inlet holes etch for XeF_2 25

Figure 23. XeF_2 etch bulk silicon 25

Figure 24. Measured Resistance values in ohms for L = 50 μm , W = 10 μm 26

Figure 25. Probe connections to sensor array and diaphragm deflection observed under probe station 26

Figure 26. SEM of piezoresistors before and after 15 cycles XeF_2 etch 27

Figure 27. Array design and metal/contact cut overlap changes 28

Figure 28. Process G1L2 wafer post wafer-saw 30

Figure 29. Poly line-resistor etching issue 31

Figure 30. SEM showing insufficient overlap of Al over the contact cuts 31

Figure 31. Epoxy cover before XeF2 32

Figure 32. Epoxy cover after XeF2 etch 33

Figure 33. Sensor array with epoxy covering line-resistor contacts 33

Figure 34. Probe station connections 34

Figure 35. Probe connections on diaphragm 34

Figure 36. Typical grain of salt placed on a diaphragm 37

Figure 37. Smallest grain of salt placed on a diaphragm 38

Figure 38. Metal ball placed on a diaphragm 38

Figure 39. Probe tip pushdown on diaphragm 39

Figure 40. Probe knob rotation w.r.t a reference point 40

Figure 41. Change in output voltage observed 40

Figure 42. Marking angles on protractor by rotating probe knob 41

Figure 43. Graph for displacement of every degree turn for both calibrations 42

Figure 44. Graph for deflection w.r.t pressure applied 43

Figure 45. Graph for Vout vs Degree Turn 44

Figure 46. Graph for Vout vs Pressure 44
Figure 47. G1L1 PCB layout 47
Figure 48. 4x6" CAD layout of PCB mask consisting of G1L1 (left) and G1L2 (right) designs 48
Figure 49. Copper boards after wet Cu etch 49
Figure 50. PCBs ordered via pcbway 50
Figure 51. Fusion360 layout for CNC machine to cut individual PCBs 51
Figure 52. Wire bonding 51
Figure 53. Individual PCBs after CNC milling and drilling 51
Figure 54. Back view of final packaged sensors 52
Figure 55. Front view of final packaged sensors 52
Figure 56. Wet test setup - Dielectric liquid 53
Figure 57. Bubble formation through air injection 54
Figure 58. Boiling setup schematic 54
Figure 59. Proposed Surface Micromachining Process flow 58
Figure 60. cont. Proposed Surface Micromachining Process flow 59

List of Tables

Table 1. Theoretical pressure exerted by a bubble of given diameter 19

Table 2. Design comparison between G1L1 and G1L2 devices 29

Table 3. Resistances corresponding to probe connections 35

Table 4. Diaphragm 6 Vout w.r.t probe connections 35

Table 5. Diaphragm 7 Vout w.r.t probe connections 35

Table 6. No pressure Vout 36

Table 7. Mass required for given pressure 37

Table 8. Output voltage observed across V1 and V2 with probe pushdown 40

Table 9. Output voltage change with further probe pushdowns 40

Table 10. Normalized Vout of S1, S2, S3 compared to target Vout 43

1.0 Introduction

As technology is advancing due to continuous research, the inception of more compact, efficient,and powerful devices is observed. However, heat rejection from such devices becomes ever so critical in maximizing their potential, and hence efforts need to be laid to improve the current cooling techniques. Microelectronic devices, servers, supercomputers, power plants, and boilers are some of the equipment which can benefit from improved two-phase heat transfer across their respective boundary layers. Hence, effective means to find out better cooling techniques is the requirement of the hour.

1.1 Boiling Fundamentals

Out of all the various techniques applied to cool a device, boiling becomes the more effective one [1]. Boiling is a two-phase heat transfer mechanism that takes advantage of the latent heat of evaporation and specific heat, making it a more efficient form of heat transfer. Boiling is a phase change process that takes away heat in high fluxes as it converts the liquid into vapor. The boiling process consists of nucleation in the liquid cover cavities on the heater surface, bubble inception, bubble growth, and bubble departure from the heating surface to the liquid-gas interface and subsequent bubble collapse [2]. There are two modes of boiling: Pool Boiling & Flow Boiling.

Pool boiling: It is boiling from a heated surface submerged in a large volume of stagnant liquid. Pool boiling takes place in 4 phases: free convection region, nucleate boiling region, transition boiling region, and film boiling region. Schematic of various stages of pool boiling is shown in below Figure 1.

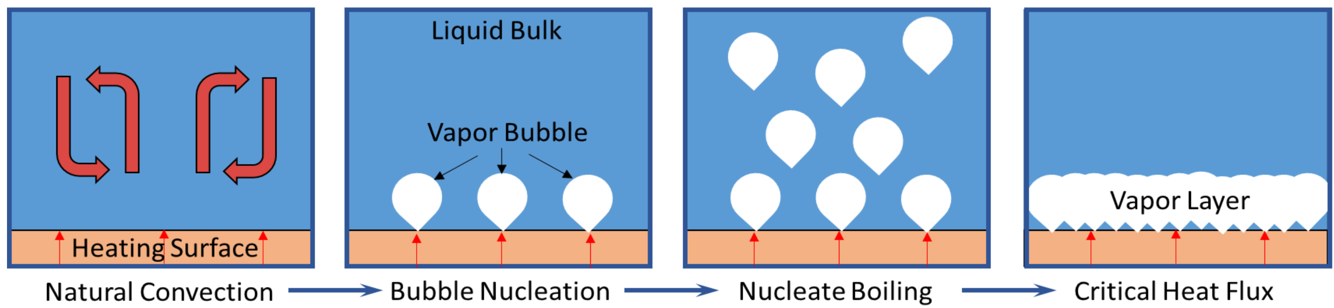

Figure 1. Pool boiling phases

Convection region is where the heat transfer takes place between heating surface and water due to natural convection. In nucleate boiling, bubbles are formed at the bottom heating surface. These bubbles develop and detach, and more heat is carried away by the liquid. Bubbles reach the free surface where they break up and release their vapor content. Further increasing the supply of heat flux to the heating surface, the vapor bubble grows in size and starts coalescing, and consequently, fully developed nucleate boiling is observed. The coalesced bubbles form a column-like structure above the heating surface carrying a large amount of heat with them. Pool boiling reaches a point of Critical Heat Flux (CHF) where the heated surface is completely covered with vapor film which acts as an insulator and radiation heat transfer takes place as a result. This suddenly decreases the efficiency of heat transfer, thus causing localized overheating of the heating surface [3]. Eventually, upon gradual cooling of the heating surface, we can trace back to nucleate boiling region. To improve the boiling performance, a reduction in wall superheat in the nucleate boiling region, an increase in CHF, or both are desired. Thus, boiling maintains low surface temperatures by dissipating high heat flux.

Flow boiling: Flow boiling occurs when a fluid circulates over a heated surface by external means such as a pump or due to the natural buoyancy effect. The heat transfer performance in the pool boiling systems is considerably lower than that in the flow boiling systems. We can enhance pool boiling heat transfer with a simple add-on tapered manifold over a plain surface to convert pool boiling into flow boiling.

1.2 Conversion of Pool boiling to Flow boiling

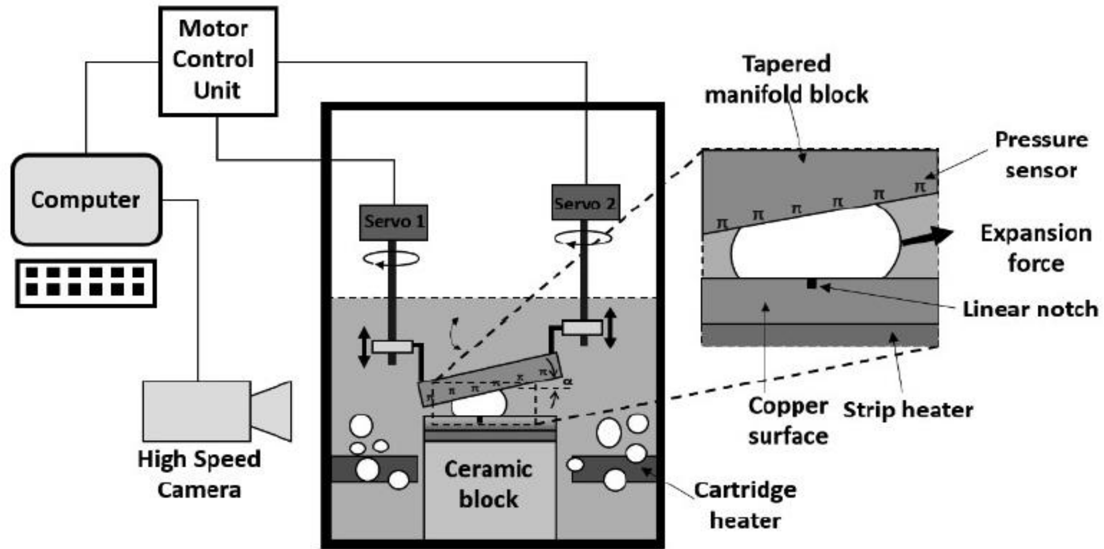

Figure 2. Schematic of proposed experimental setup for studying bubble squeezing mechanism in tapered micro-gap by Kandlikar et al. [17]

Bubbles are the result of expansion of a liquid into its vapor phase. Pressure buildup in the bubble due to the squeezing mechanism near the inlet is identified as the main driving force in the tapered micro-gap. By adding a tapered manifold block on top of the heating surface, the expanding bubbles create unidirectional self-sustained liquid streams. The pressure recovery in the expanding micro-gap reduces the flow resistance and helps in establishing a self-sustained two-phase flow. The forces from bubbles growing can provide a pumpless, sustained unidirectional flow effectively transforming pool boiling into extremely efficient flow boiling. This study will provide an insight into the interfacial transport and bubble motion in micro gaps. Through this study, we can achieve improved CHF, and HTC performance than commercial air and water coolers [17]. The applications of this study will result in energy savings, and it will improve the reliability and performance of electronic equipment. Schematic of the proposed experimental setup for studying bubble squeezing mechanism in tapered micro-gap is shown in above Figure 2.

1.3 MEMS Piezoresistive Pressure Sensors

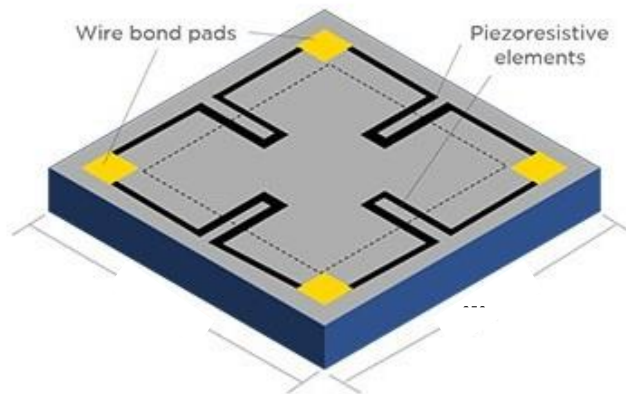

Figure 3. MEMS Pressure Sensor model adapted from [4]

Among the very first micromachined device developed in production quantities was the piezoresistive pressure sensor. From the automobile industry to the medical industry, pressure sensors have a multitude of purposes including airbag systems and ventilators. There are two key components of a traditional pressure sensor: a diaphragm and resistors [4]. For pressure sensors, silicon is used because it incorporates well-established electronic properties and superior mechanical properties. Significantly reduced dimensions and weight, batch processing and simple interfacing with electronic circuits and microprocessors are other benefits of silicon. Figure 3 shows the model of a MEMS pressure sensor.

This project is aimed at understanding the forces and fundamental mechanisms governing the pressure field and interface motion around nucleating and growing bubbles in a tapered micro-gap and the resultant unidirectional fluid pumping. This will be achieved through pressure field mapping around the bubble with MEMS piezoresistive pressure sensor array.

Two types of fabrication techniques are used: Bulk Micromachining and Surface Micromachining. In Bulk micromachining process, the structures are created inside the silicon substrate, whereas in Surface micromachining, the structures are created on top of Si substrate. Surface

Micromachining offers several advantages in comparison to Bulk Micromachined pressure sensor: smaller size, better dimensional control, and compatibility to CMOS technology. The Bulk Micromachining is a straightforward and well-documented process, whereas Surface micromachining needs complex mask designs and is an intricate process. Also, the Bulk Micromachined sensors have better mechanical properties, and it is a well-developed technology.

The pressure sensor consists of a thin square diaphragm formed by etching the Silicon. The diaphragm performs mechanical stress amplification. The thin diaphragm will curve downwards or upwards, suggesting traction or compression on the piezoresistors when a pressure differential is exerted through the unit. The piezoresistors are connected in a Wheatstone bridge configuration. Thus, any deflection on the two sides of the diaphragm due to pressure changes can cause either compressive or tensile stress on the resistors, marginally altering their resistances. The difference in resistor values and the pressure applied to the diaphragm have a clear relationship. Application of pressure on the diaphragm creates deflection proportional to pressure difference. The unique challenges involved in the fabrication of sensors for this project are the required hypersensitivity of 100 μV / 20 Pa, designing an array of sensors to measure the pressure at various stages of bubble growth, size limit and measurement of pressure in a liquid pool. Some attempts have been made at fabricating pressure sensor arrays [5], but they are generally in a much larger scale and targeted at higher pressures (>100kPa). Hence, a unique process flow was developed to achieve the required thinness of diaphragm based on the calculations.

2.0 Literature review

The following sections will briefly discuss the relevant work done by other researchers to understand the design considerations and optimization of pressure sensors.

2.1 Piezoresistive Effect

The piezoresistive effect is the change in a material's resistivity caused by a strain application. In semiconductors, the known phenomenon is very enormous. Although the strain that can be incorporated into a crystal is typically minimal, only the linear principle of the resistivity-strain relationship is of concern [6]. The most general linear dependence of the stress-caused shift in resistivity is given by:

$$\Delta\rho_{ij} = \sum_{k,l} \pi_{ijkl}\sigma_{kl} \tag{1}$$

where $\Delta\rho$ is the change in resistivity caused by applied stress, π_{ijkl} are the piezoresistive coefficients, and σ is the stress. . In general, the piezoresistive effect is created by the modification of energy band structures by applied strain, thereby leading to changes in the effective mass, mobility, and conductivity [7]. The resistivity in a crystalline material changes because carrier mobility changes due to the deformation of the atomic structure of the semiconductor when under strain. The silicon lattice is not an isotropic structure. Therefore, the direction of the strain will determine the change in resistance. The gauge factor is used to characterize the piezoresistors sensitivity; GF is defined as the ratio of relative change in electrical resistance and the mechanical strain. For a single-crystal Si in certain directions, such as the (110) direction, the GF lies between 50 and 100. Similarly, the discovery of the PZR effect in polycrystalline Si (polysilicon) in the 1970s [8,9] facilitates its sensing applications [10,11]. The polysilicon as a piezoresistive material instead of the single-crystalline Si offers the advantages of low cost, ease of processing, and good thermal stability, and p–n junction isolation is not

necessary even though its GF value is lowered. The polysilicon GF depends on the doping concentration and is lower than crystalline silicon. The gauge factor G can be obtained from the following relationship shown in Equation (2)

$$G = \frac{\Delta R/R}{\varepsilon} \tag{2}$$

$$G = \frac{(R_{(\varepsilon)} - R_0)/R_0}{\varepsilon} \tag{3}$$

Where, $R_{(\varepsilon)}$ is the resistance of strain gauge at strain ε and R_0 is the resistance of strain gauge at zero strain.

Placement of resistors on top of the diaphragm is very important. In order to achieve an optimal configuration, as pressure is applied, these resistors must be positioned where the stress on the diaphragm is greatest. The stress is directly proportional to the pressure applied on a square diaphragm and is given as follows .

$$\sigma = (0.3)\left(\frac{L}{H}\right)^2 * P \tag{4}$$

where σ is the stress is, L and H are the diaphragm length and thickness, and P is the pressure applied. Knowing the stress, strain can be determined using the Hooke’s law. Strain offers information about how, with applied stress, the dimensions of the polysilicon resistors change.

$$\varepsilon = \frac{\sigma}{\mathrm{E}} \tag{5}$$

where ε is the strain, E is the Young’s Modulus.

The resistance of any given resistor of length L and width W is given by Equation (6).

$$\mathrm{R} = R_s \frac{L}{\mathrm{W}} \tag{6}$$

where R_s is the sheet resistance.

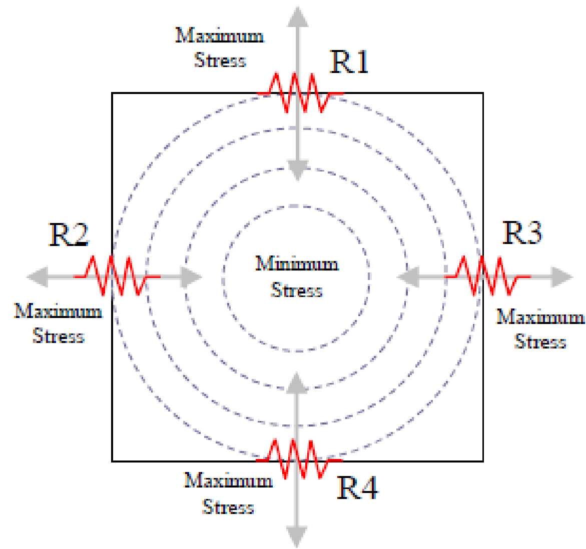

Figure 4. Areas of maximum stress on square diaphragm

The middle of the square diaphragm is the center of stress. The stress is transmitted from the middle radially outward and it is shown in Figure 4 as the red lines. The maximum deflection Y_{max} at the center of the diaphragm is given as follows.

$$Y_{max} = \frac{0.0151 * P * L^4 (1 - Nu)^2}{EH^3} \tag{7}$$

where P is the applied pressure, L is the length of the side of the square diaphragm, Nu is the Poisson's ratio and H is the diaphragm thickness. At the four points where the red lines intercepts the diaphragm tip, the highest stress will occur. Thus, the piezoresistors will be positioned as close to these points as possible.

2.2 Wheatstone Bridge

A common improvement to the sensing capabilities of a piezoresistive diaphragm is to use a Wheatstone bridge where the elements in each pair are subjected to equal and opposite strain as shown in Figure 5. This increases the output signal while reducing the effects of temperature and other environment variables. The Wheatstone bridge and 1-turn resistors improve sensitivity. The issue to be considered here is the feasibility of implementing this design with the extremely small size of the sensors being fabricated for this project.

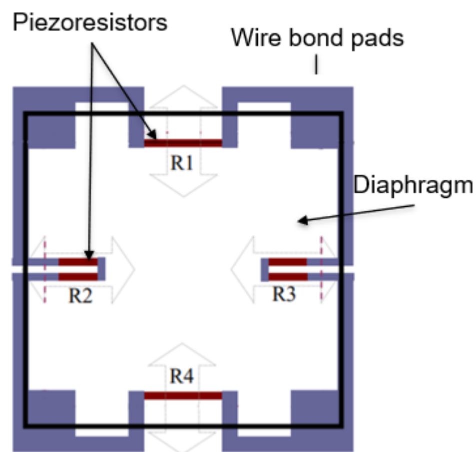

Figure 5. Schematic of piezoresistors in Wheatstone bridge configuration

Sir Samuel Hunter Christie invented this design in 1833 and Sir Charles Wheatstone enhanced it and revolutionized it in 1843 [12], [13] he used the device to be able to analyze and compare the results from different soils. The main purpose of the Wheatstone bridge is defined as a 'differential resistance measurer', used to distinguish the resistance for an unknown value on one of the branches. Two resistors are oriented so that stress can be sensed in the direction of their present axes, and two are positioned perpendicular to their current flow to measure stress. The resistance shift of the first two piezoresistors would thus still be counter to that of the other two. By positioning two piezoresistors parallel to opposite diaphragm edges and the other two perpendicular to the other two edges, this is done. The parallel resistors are under lateral stress and indicate a decrease in resistance as the

diaphragm is bent downward. This causes tensile stress on the diaphragm surface at the sides, whereas the perpendicular ones are under longitudinal stress and display an increase in resistance. Below Figure 6 is an overview of a design of a Wheatstone bridge circuit.

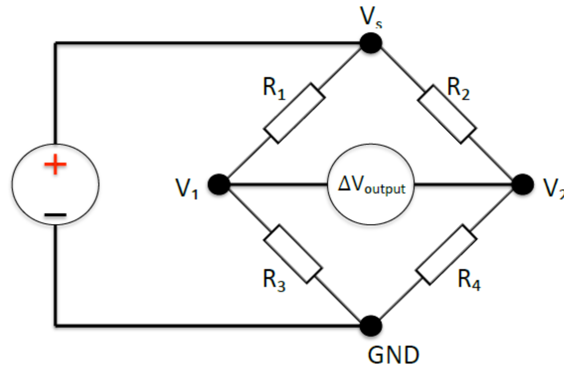

Figure 6. Design of Wheatstone bridge circuit

Normally, R4 would be the unknown resistance value, but this depends on the user's approach. In the case R4 is the unknown value, assumptions are made, first we have to balance the entire circuit, it occurs when:

$$\Delta V = V_2 - V_1 = 0 \tag{8}$$

$$V_2 = V_1 \tag{9}$$

Then the circuit gets analyzed using Kirchhoff's Current Law (KCL), shown in Eq. 10, where the sum of all currents going in are equal to those leaving a node. By applying this law and assessing just like shown in Figure 7:

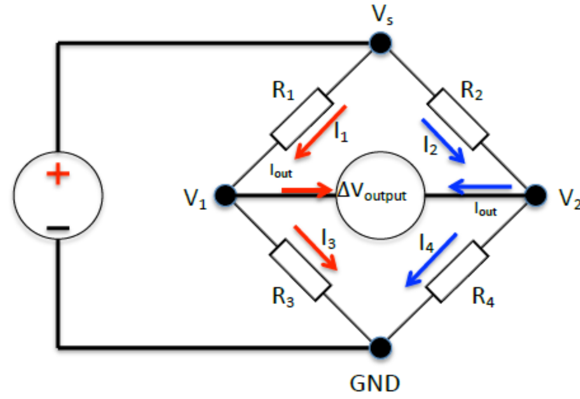

Figure 7. Applying KCL to the Wheatstone bridge

$$\sum_{k=1}^{n} I_k = 0 \tag{10}$$

where k represents the nth number of nodes, and n is the total number of currents going in or leaving the node in question. Above in Figure 7, by analyzing the nodes in V1 and V2 we find:

At Node V_1 we have: $$I_1 - I_3 - I_{output} = 0 \tag{11}$$

Or $$I_3 = I_1 \text{ assuming } I_{output} = 0 \tag{12}$$

At Node V_2 we have: $$I_2 - I_4 + I_{output} = 0 \tag{13}$$

Or $$I_2 = I_4 \text{ assuming } I_{output} = 0 \tag{14}$$

Now applying Kirchhoff's Voltage Law (KVL) shown in Eq. 15, it is possible to find a couple of voltages from every resistor and given currents. So, applying this at nodes V1 and V2.

$$\sum_{k=1}^{n} V_k = 0 \tag{15}$$

Using Ohm's law:

$$I = \frac{V}{R} \rightarrow V = IR \tag{16}$$

At Node V_1 we have: $$(I_1R_1) - (I_3R_3) - (I_{output}R_{output}) = 0 \tag{17}$$

At Node V_2 we have: $$(I_2R_2) - (I_4R_4) + (I_{output}R_{output}) = 0 \tag{18}$$

Now that the circuit is balanced, assuming the bridge gets balanced, thus $V_{output} = 0$, will give

$I_{output} = 0$ amperes. Both sets of new equations are placed equal which satisfy the assumption from Eqs. 12 and Eqs. 14:

$$(I_1R_1) - (I_3R_3) - (0) = 0 \quad (19)$$

$$(I_1R_1) = (I_3R_3) \quad (20)$$

and

$$(I_2R_2) - (I_4R_4) + (0) = 0 \quad (21)$$

$$(I_2R_2) = (I_4R_4) \quad (22)$$

Now, look for the value of R_4 by setting Eqs. 20 and 22 equal to each other:

$$(I_1R_1)(I_4R_4) = (I_3R_3)(I_2R_2) \quad (23)$$

Using KCL assumptions from Eqs. 12 and 14

$$I_3 = I_1 \text{ and } I_2 = I_4 \quad (24)$$

R_4 can be reduced to resistor values:

$$R_4 = \frac{(R_2)(R_3)}{(R_1)} \quad (25)$$

with the known values of R1, R2, and R3 it is possible to calculate the value of R4 when this type of electrical circuit is chosen.

On the other hand, if R1, R2, R3, and R4 are known, together with the applied voltage then the bridge can be used to obtain the voltage difference between nodes V1 and V2, which is the main objective of the bridge for this device. This can be obtained in the following form and knowing the previous mathematical explanation:

$$V_{output} = V_2 - V_1 \quad (26)$$

At node V2:
$$V_2 = \frac{(R_4)}{(R_2+R_4)} * V_s \quad (27)$$

At node V1:
$$V_1 = \frac{(R_3)}{(R_1+R_3)} * V_s \quad (28)$$

Therefore, we get:

$$V_{output} = \left(\frac{R_4}{R_2 + R_4}\right)V_s - \left(\frac{R_3}{R_1 + R_3}\right)V_s$$

$$V_{output} = \left[\left(\frac{R_4}{R_2 + R_4}\right) - \left(\frac{R_3}{R_1 + R_3}\right)\right]V_s \tag{29}$$

Finally, substituting the known values with their respective coefficients, we can obtain the relative voltage output at given nodes V2 and V1.

For purposes of the sensor used in this study, the style of circuit used is very similar to the one presented in Figure 6, which shows four resistors arranged as two parallel branches with two resistors in series in each branch. A voltage difference can be recorded through the use of two probes on nodes V1 and V2, and the opposite sides from where the +5V (Vs) and ground (GND) connections are found. The main purpose for this circuit is to be able to measure the voltage difference found in the stress of the resistors as the diaphragm deflects, this in other words is the measurement of the root mean squared (RMS) of the voltage difference.

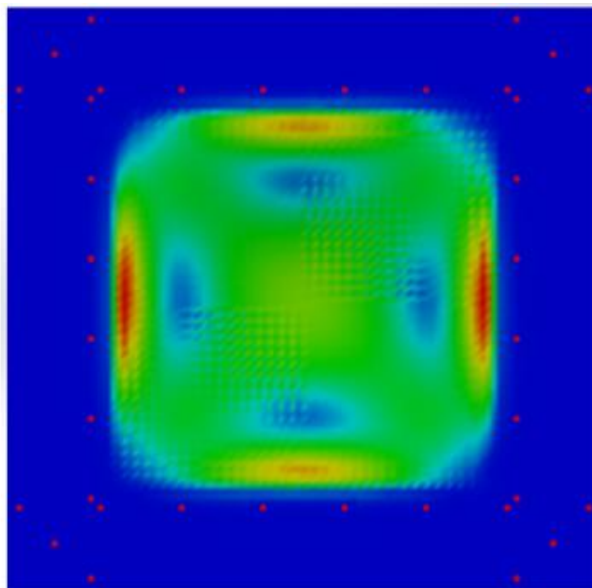

Figure 8. Solidworks simulation of square diaphragm of L=200μm and H=1μm

The voltage is sensed by the resistors, which happen to be located where most of the stress occurs on a diaphragm as shown in Figure 8. The image above relates the dimensions used in the sensors. This simulates the stress locations on the diaphragm and is a suitable way to help place the resistors on these exact locations (red) where most of the stress is located, similar to various square pressure sensors.

2.3 Design Optimization using Taguchi Approach

M. Mohamad et. al [14] conducted a study to understand the factors influencing the sensitivity and linearity of the pressure sensors. Diaphragm thickness, the shape and placement of the piezoresistors, and the doping concentration were the factors that were incorporated and tested to obtain higher sensitivity in silicon-based piezoresistive intracranial pressure sensor, while maintaining the linearity of the sensor. The sensitivity of the existing MEMS piezoresistive intracranial pressure sensors are in the range of 100 µV/6.65 kPa to 100 µV/78.2 Pa (2 µV/V/mmHg to 0.17 mV/V/mmHg). COMSOL simulation results indicated that diaphragm thickness, and perpendicular piezoresistors play an important role.

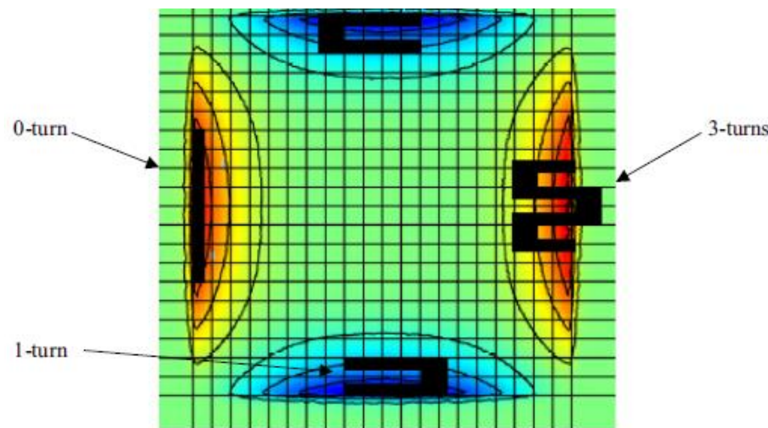

Figure 9. The placements of 0-turn, 1-turn and 3-turns piezoresistors on the high stress region, i.e. within the diaphragm [14]

The centers of edges of the diaphragm are experience higher mechanical stress compared to the central point. The four piezoresistors were positioned within the confinement of the diaphragm, indispensably at the center of the diaphragm's edges as shown in Figure 9. Doping concentration of piezoresistors also has a significant impact on linearity performance. It was observed that a square diaphragm had 60% higher stress than circular of the same thickness. This study has adopted the Taguchi method using four substantial factors to obtain an optimized design for a silicon-based sensor.

The factors used by this study are the diaphragm thickness (A), the type of perpendicular piezoresistors (B), the type of parallel piezoresistors (C), and the piezoresistors' doping concentration (D).

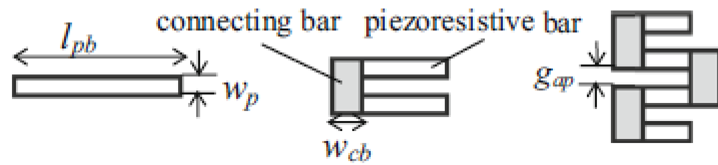

Figure 10. Meander shaped piezoresistors. 0-turn, 1-turn and 3-turns [14]

The preferred choice was using p-type piezoresistors oriented along <110> direction on (100) plane. And hence the optimum design would be three turns perpendicular and zero turns parallel meander shaped piezoresistors of $10^{17} cm^{-3}$ doping concentration on a 2μm thick diaphragm. Also, to maintain high linearity, Pressure vs Output Voltage, they observed that low doping concentration of around 10^{15} cm^{-3} , and one turn resistors can be used. The 0-turn, 1-turn and 3-turns meander shaped piezoresistors are shown in above Figure 10. Also, the thinner diaphragm was subjected to a larger mechanical stress, which led to better sensitivity.

3.0 Objectives & Calculations

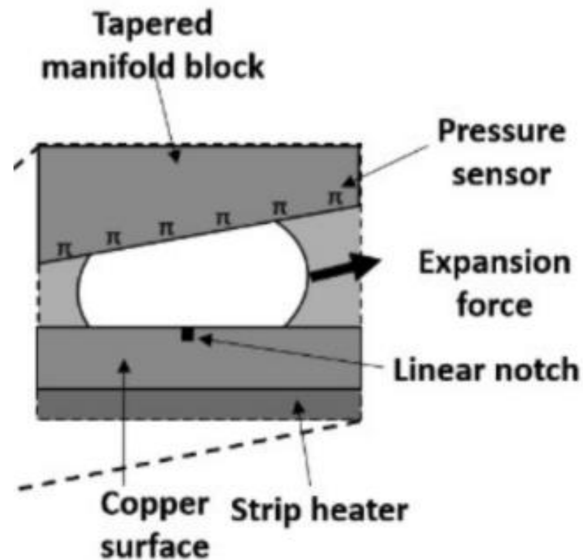

Figure 11. Proposed bubble squeezing mechanism by Kandlikar et al. [17]

To develop hyper-sensitive (100 µV / 20 Pa) MEMS based pressure sensors of diaphragm length L = 200 µm x 200 µm, 0.75 µm to 0.225 µm thick, that will allow effective measurement of the pressure exerted (20 Pa to 1 kPa) by a nucleating bubble of Diameter: 200 µm to 10 mm, in a pool boiling environment.

Designing an array to measure pressure at various stages of bubble growth as it travels along the length of the tapered manifold as depicted in Figure 11. The total distance travelled by the bubble will be around 8mm. The sensor array must not obstruct the formation of the bubbles and should allow smooth flow of the bubbles. Also, characterizing the performance of the sensors.

The final packaged sensors must be compatible with the dielectric wet test setup. And the packaged sensors will be provided for pressure sensing when submerged inside a dielectric fluid.

Bubble Pressure Calculations:

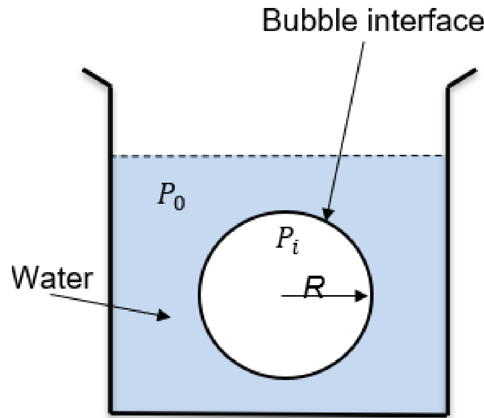

Figure 12. Schematic of a bubble in water

The pressure exerted by a nucleating bubble in water can be determined using the following equations.

Surface Tension of water at 100^0C [15]: $\sigma = 58.9$ mN/m

The maximum bubble diameter in boiling water over a plain copper chip is D = 2.5 mm

Let P_0 = Pressure outside bubble (liquid pressure),

And P_i = Pressure inside bubble

Using the force balance equation at the bubble interface shown in Figure 12, and reducing the equation:

Balancing force at bubble interface [16]

$$P_i\,\Pi R^2 = P_0 \Pi R^2 + \sigma 2\pi R \tag{30}$$

Reducing the equation, we get:

$$P_i - P_0 = \frac{2\sigma}{R} \tag{31}$$

Here, $P_i - P_0$ can also be called as gauge pressure.

Substituting the values in eq (31), we get:

$$P_i - P_0 = 94.24 \text{ Pa} \tag{32}$$

The surface tension values changes with liquid and its temperature.

Thus, a bubble of diameter of 200μm would give a theoretical pressure exerted of 1 kPa and a bubble of 10mm diameter would exert a pressure of 20 pascals.

Bubble Diameter	Pressure Exerted (Theoretical)
200 μm	1 kPa
2.5 mm	94 Pa
10 mm	20 Pa

Table 1. Theoretical pressure exerted by a bubble of given diameter

Target Voltage Sensitivity of ΔV = 100 μV for pressure of P = 20 Pa with supply voltage V_{DD} = 5 V.

Dimension constrains: Length of square diaphragm L= 100 to 200 μm , thickness H= 0.75 to 0.225 μm to achieve desired sensitivity.

<u>Design calculations</u>:

It is assumed that the pressures reached within the tapered microgap will be in the range of 20 Pa to 1 kPa and will not exceed 1 kPa. Given the expected values, a target minimum sensitivity is set for the sensors at a pressure P = 20 Pa and a voltage output of ΔV = 100 μV,

With an input of V_{DD} = 5V, the change in resistance *ΔR* for any given resistor *R* in a Wheatstone bridge configuration can be found from:

$$V_{out} = V_2 - V_{1-} = V_{dd}\frac{\Delta R}{R} \tag{33}$$

By substituting the values in above equation, we get $\Delta R/R = 20 \times 10^{-6}\ \Omega$

The strain needed on polysilicon piezoresistors, assuming Gauge Factor of 10, can be determined using Equation (2).

For lightly doped polysilicon resistors with Young's modulus of 140 GPa, a corresponding minimum stress needed to detect 20 Pa of pressure is calculated to be 3.3×10^5 Pa. The dimensions of the square diaphragm: length L and thickness H, needed to produce this minimum stress can be calculated using Equation (4).

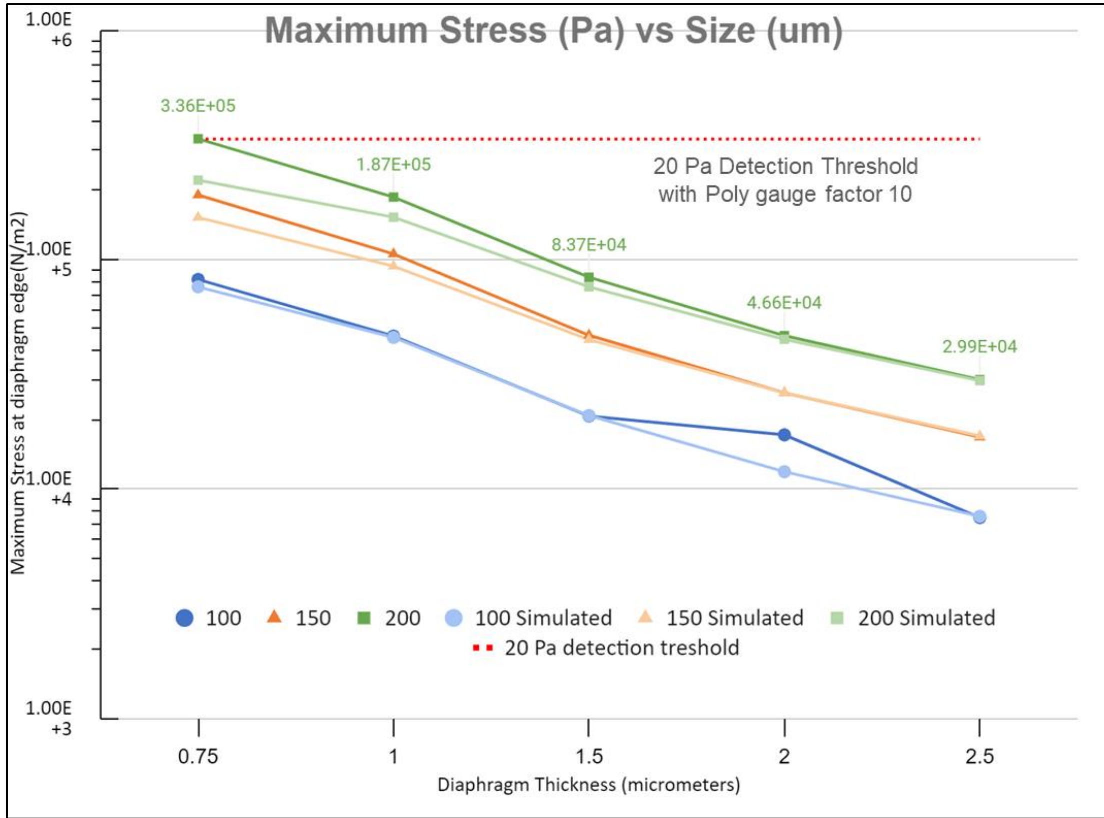

Figure 13. Maximum predicted stress at diaphragm edge vs. size of diaphragm

With the Eq. (4) for stress, calculations were performed on various diaphragm sizes and thickness, and compared with the target sensitivity as shown with the dark solid lines in Figure 13. COMSOL simulations were used to extract the maximum stress on a silicon nitride diaphragm of the corresponding dimenstions, and are also plotted as light colored solid lines as shown in Figure 13. The Figure 13 shows that the calculated values (dark) are slightly higher than the simulated values (light). Also shown in Figure 13 is the horizontal red dotted line representing the minimum stress needed at the center of the edge of the diaphragm to detect a pressure of 20 Pa, assuming a polysilicon gauge factor of 10.

Based on the results presented in Figure 13, a size of L = 200 µm with a target thickness of <0.75 µm was selected for the square diagrams.

4.0 Bulk Micromachining Process

4.1 Gen1 Lot1 Devices

4.1.1 Initial Sensor Design

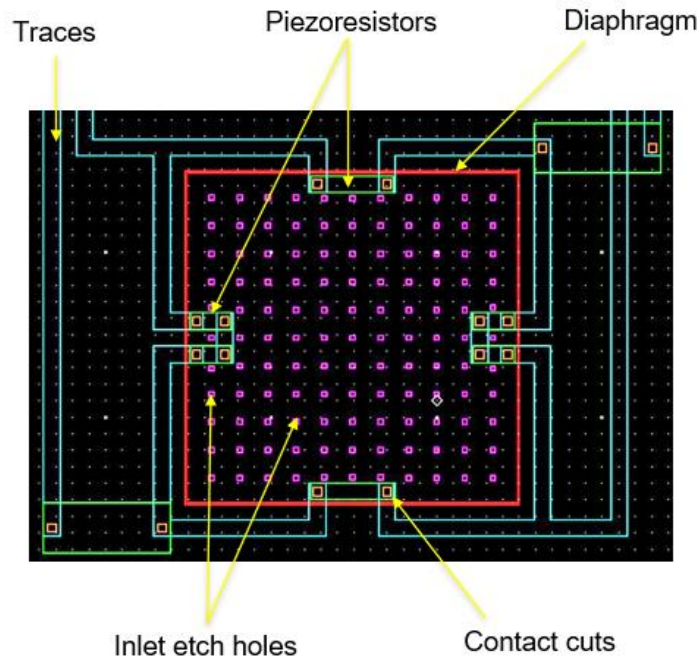

Figure 14. G1L1 pressure sensor layout

The Bulk Micro-Machining process includes a diaphragm of area 200μm by 200μm. There are four piezoresistors on top of the diaphragm with total length of 50μm and width of 10μm. The area of the contact cuts is of 5μm by 5μm and XeF2 inlet etch holes on top of the diaphragm are 3μm by 3μm wide. Trace width of aluminum is of 10μm. For the mask layout, we chose a die size of 10mm by 10 mm. The mask layout has alignment marks and test features on top. Each die has three rows of sensor arrays, and each sensor array has five diaphragms at 80μm apart from each other. All sensor arrays have a length of 2000μm and width of 500μm. The street width between the two arrays is 200μm. Aluminum contact pad area is 150μm by 150μm and for the wafer saw the X-axis index is 0.7 mm and the Y-axis index is 3.2 mm. The G1L1 pressure sensor layout is shown in Figure 13. The sensor array and mask layout of a single die is shown in Figure 14 (a) and (b).

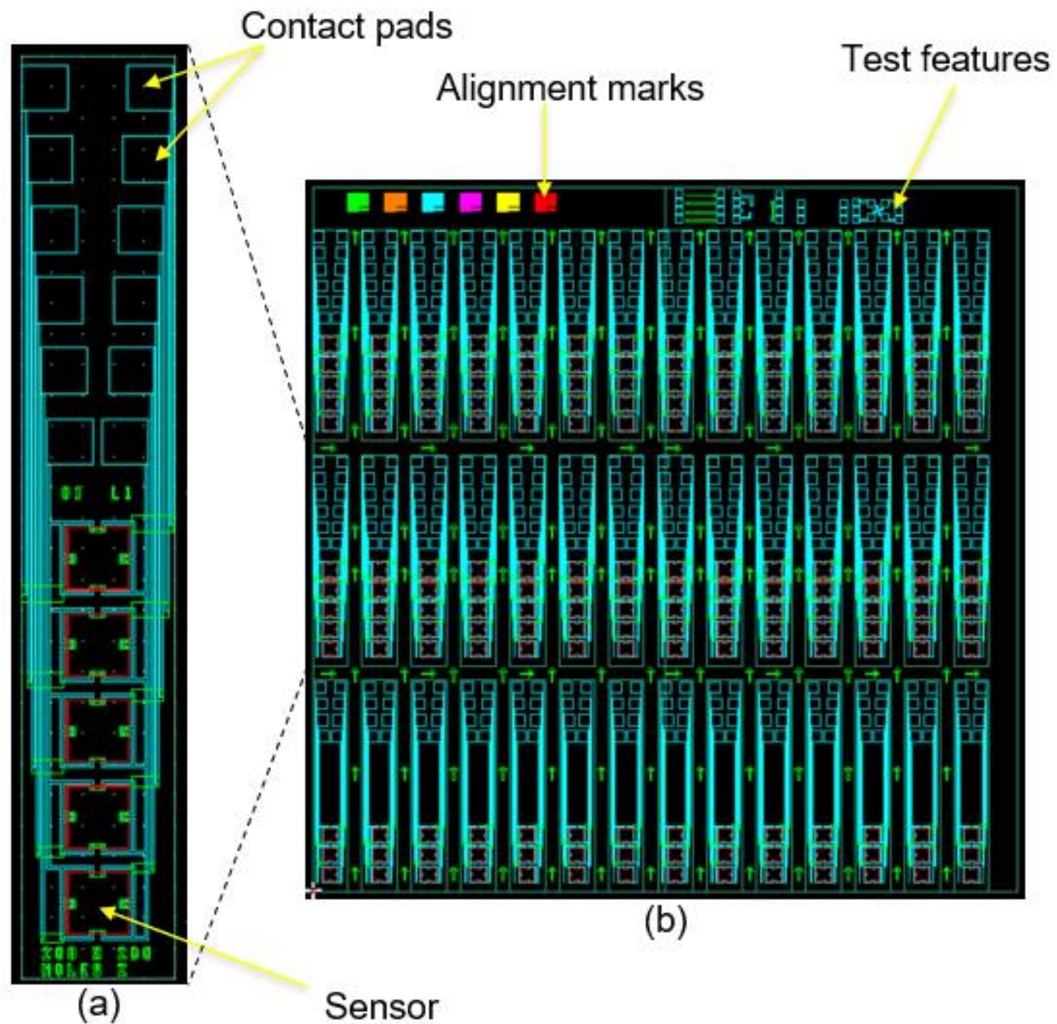

Figure 15. (a) Sensor array layout, (b) Mask layout of single die

4.1.2 Fabrication G1L1

A process flow for bulk micromachined sensors was developed showing the cross section of a device at various points throughout the process. Fabrication was completed at the Semiconductor and Microsystems Fabrication Laboratory (SMFL), located at RIT. This process includes a front side XeF_2 diaphragm etch. Full process details are listed in Appendix.

The RIT top-side bulk micromachined MEMS process flow starts with 6” n-type wafers. After a RCA clean, alignment marks are patterned and etched followed by another RCA clean. 1000 Å of SiO_2 is grown on top of the wafers in the Bruce Furnace as depicted in below Figure 15.

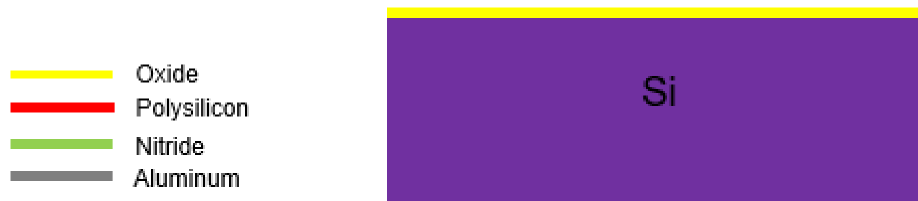

Figure 16. Grow dry oxide on (100) Si wafers

Using Low Pressure Chemical Vapor Deposition, 4500 Å of polysilicon is deposited as shown in Figure 16.

Figure 17. LPCVD Polysilicon

Borofilm 150 is then spun onto the wafer, and the wafers are baked at 200^0 for 20 mins. Next the wafers are put into a diffusion furnace to dope the exposed areas with boron. Once the diffusion step is complete, all the Borofilm and existing oxide is etched away using BOE. Sheet Resistance of the doped polysilicon is measured using the Resmap. This polysilicon is then patterned with the first photolithography step and etched in the LAM490 tool. A stress relief oxide layer is grown followed by 3000 Å Low Pressure Chemical Vapor Deposition (LPCVD) of Si_3N_4 as shown in Figure 17. This nitride layer will be used in the future as diaphragm for the pressure sensors.

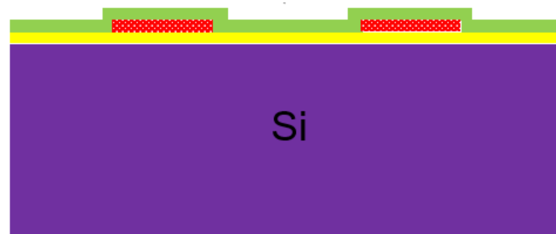

Figure 18. Polysilicon doping, patterning and LPCVD Nitride

The nitride is then patterned with the second photolithography step and plasma etched to form contact cuts on top of the polysilicon as shown in below Figure 18.

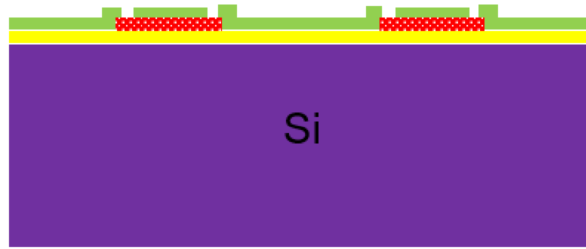

Figure 19. Contact cuts etch on Nitride

The wafers are then dipped in 10:1 BOE for 1min to remove any oxide remnants followed by a standard RCA clean. A 0.5 μm layer of aluminum is sputtered onto the front of the wafer and into the contact cuts as shown in below Figure 19.

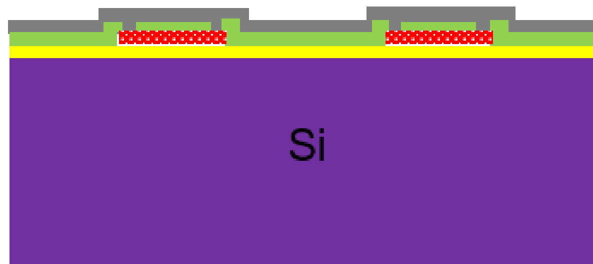

Figure 20. Aluminum sputter deposition

The aluminum is patterned with the third photolithography step and etched using an aluminum wet etch as shown in Figure 20. The wafers are etched with constant agitation for 5 minutes followed by a 5 min DI water rinse. This is followed by a 1 min freckle etch rinse to remove silicon residue left over after the etching of aluminum containing 1% silicon. The aluminum is then sintered at 200^0 for 30 mins.

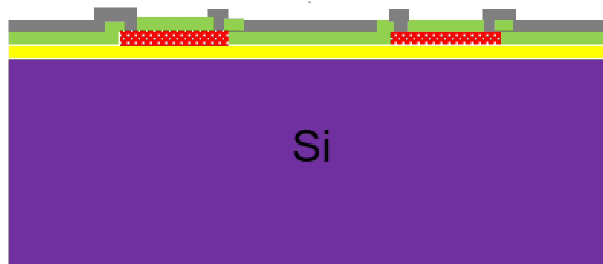

Figure 21. Aluminum wet etch

Inlet holes for etching bulk silicon are patterned with a final photolithography step. The holes are etched through nitride and oxide layers with bulk silicon underneath. These holes will act as an inlet for

the XeF_2 to etch away the bulk silicon as shown in below Figure 21.

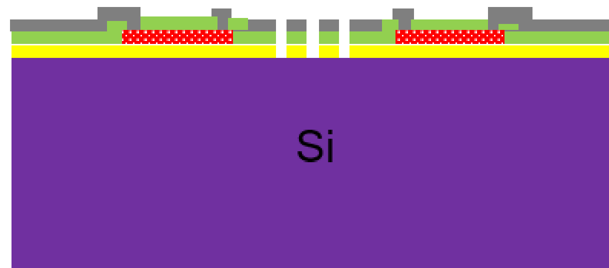

Figure 22. Inlet holes etch for XeF_2

At this point the wafers must be diced into individual die before further processing. This is necessary because the devices with diaphragms will be too delicate to dice after the XeF_2 cavity etch. After the wafers are diced, they go through the XeF_2 bulk silicon etch. This etches all way through the bulk silicon releasing the diaphragms.

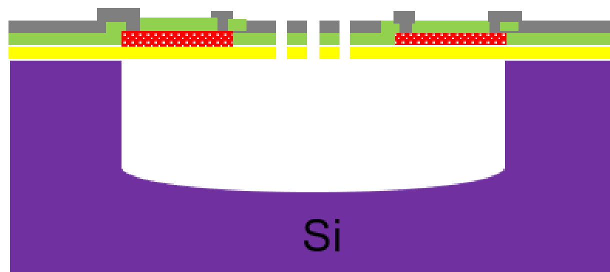

Figure 23. XeF_2 etch bulk silicon

The finished devices, shown in Figure 22, are now ready to be packaged, wire bonded, and tested.

4.1.3 Preliminary Testing

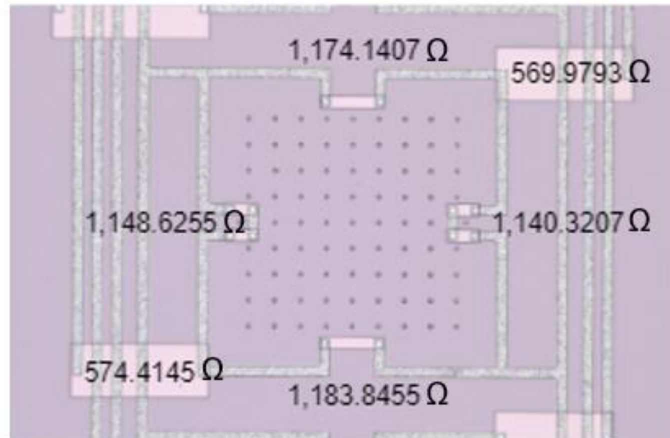

Figure 24. Measured Resistance values in ohms for L = 50 µm , W = 10 µm

Initially, resistance testing was carried out before the XeF2 cavity etch. Resmap showed Sheet Resistance Rs = 200 Ω/sq. We tested the wafer for C12 before dicing for resistances on one full array on five locations of the wafer. The dies in the center were closest to target values of 1000Ω as shown in Figure 23. The contamination from the B-150 dopant might have resulted in connection issues for some arrays. The results were consistent with our belief that the dies in the center are closest to the target values.

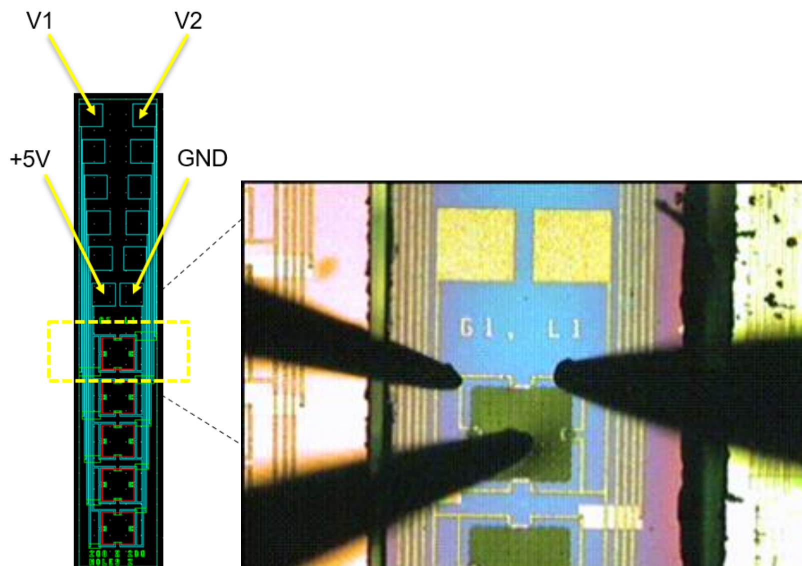

Figure 25. Probe connections to sensor array and diaphragm deflection observed under probe station

Before and after etching, the lot was tested with +5V and GND applied to the Wheatstone bridge as shown in Figure 24. Before the XeF2 etch, the diaphragms that did not have damaged connections consistently measured less than 1 mV. After the XeF2 etch, the piezoresistors were being etched and there was an open circuit issue. It was speculated that the XeF2 must have come in contact with some of the polysilicon resistors and etched it away.

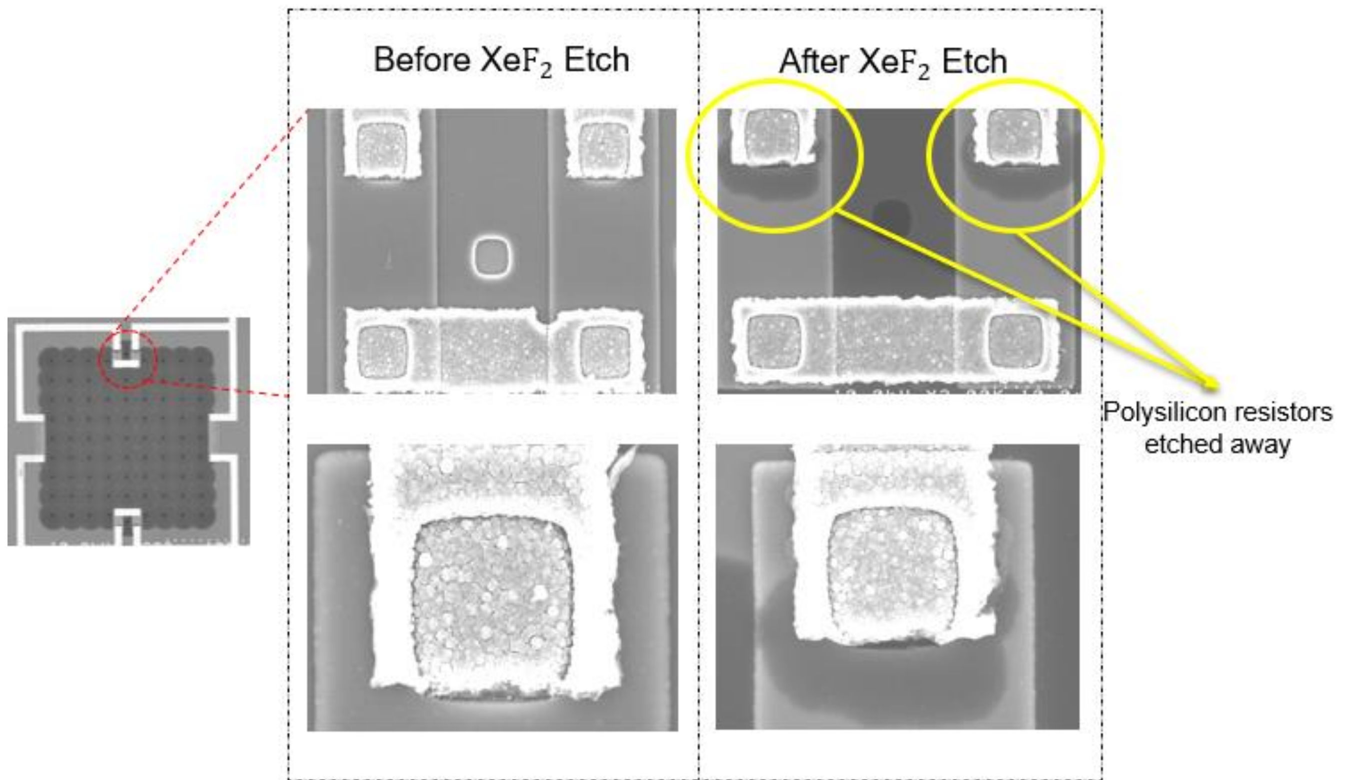

Figure 26. SEM of piezoresistors before and after 15 cycles XeF_2 etch

One sensor array was investigated under the Scanning Electron Microscope on three occasions. First was before being etched. Second was after 10 cycles of XeF_2 and third was after 15 cycles of XeF_2 to see where the damage was occurring. On the one turn sensing resistors, there is a small space where the aluminum does not completely overlap the contact cuts as seen in above Fig 25. This might have allowed the XeF_2 to begin etching the piezoresistors. The damage caused is much worse after 15 cycles, then observed after 10 cycles.

Therefore, a new set of pressure sensor arrays, G1L2, with lessons learned from the first lot were fabricated. This included increasing the length of the array to accommodate longer travel distance of the bubble and test setup. also increasing the number of diaphragms, increasing the metal overlap over contacts so that the Poly resistors are not etched away, followed by increasing the size of contact pads for ease of wire bonding and adding traces in between the contact pads.

4.2 Gen1 Lot2 Devices

4.2.1 Optimization of Array Design

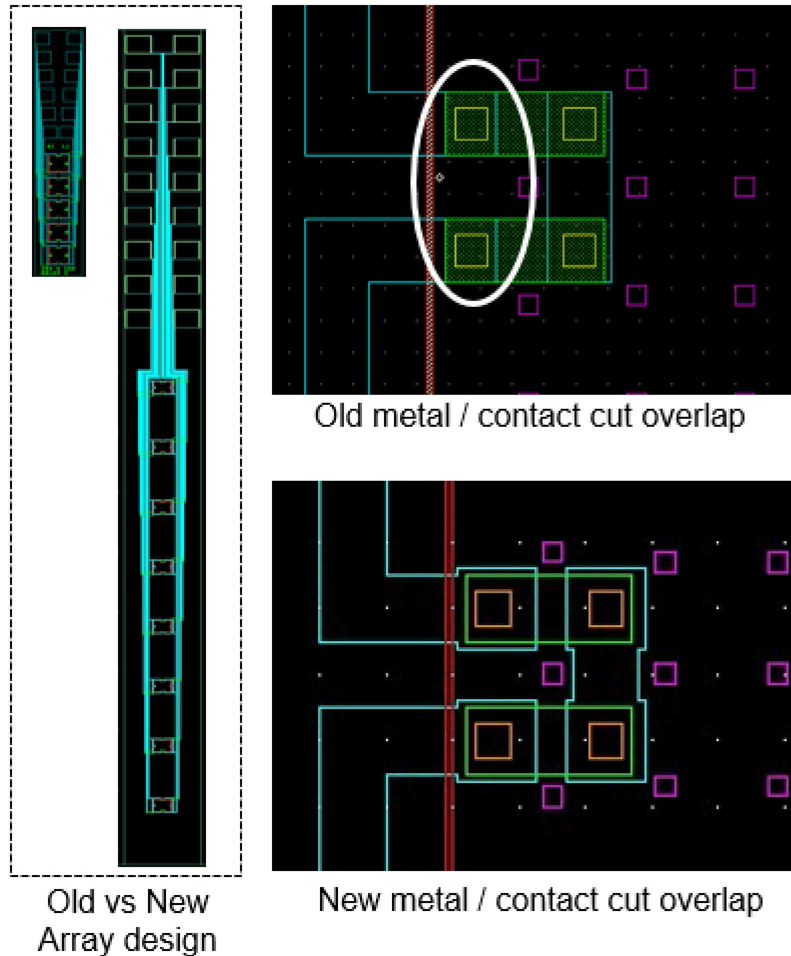

Figure 27. Array design and metal/contact cut overlap changes

In Gen1 Lot2 design, the sensor array dimensions were modified for wet test setup and the poly-resistor etching issue was resolved by increasing the overlap of the metal layer over the contact cuts as shown in Figure 26. The etch time on both the contact cuts and metal layers was reduced to prevent over-etch. The die size on Lot 2 was increased from 10mm by 10mm to 14mm by 14mm. The new array dimensions are length of 14mm and width of 500µm. The number of diaphragms were also increased from 5 to 8. The street width was the same for wafer saw with 200µm and the distance between the two diagrams was increased from 80µm to 1mm. The aluminum contact pad area was also increased from 150µm by 150µm to 300µm by 300µm. As per the new wet test setup, the total distance that the bubble would travel along the length of the array will be 8mm. Hence, 8 diaphragms are placed at a spacing of 1mm apart from each other. The G1L2 sensors were successfully fabricated with the optimized design. Below Table 2 shows the comparison between the G1L1 and G1L2 design.

	Gen 1 Lot 1	Gen 1 Lot 2
Die size	10mm x 10mm	14mm x 14 mm
Array dimensions	L = 3 mm, W = 500 µm	L = 14 mm, W = 900 µm
No. of Diaphragms	5	8
Street width	200 µm	200 µm
Distance between two diaphragms	80 µm	1 mm
Wafer Saw	x axis = 0.7 mm y axis = 3.2 mm	x axis = 14.2 mm y axis = 1.1 mm
Contact pad area	150 µm x 150 µm	300 µm x 300 µm
Distance bubble travels(sensing area)	1.5 mm	8 mm

Table 2. Design comparison between G1L1 and G1L2 devices

4.2.3 Fabrication G1L2

Due to the poly-resistor etching issue with G1L1, the top-side bulk micromachined MEMS process flow was used for a second time to fabricate a new lot of devices. The G1L2 used a slightly different process. A new stepper job was created in ASML due to a new die size of 14mm x 14mm and different die spacing for this new lot.

Experiments were performed with Spin On Doping on dummy wafers to improve low sheet resistance observed in G1L1 to a target sheet resistance of 200 Ω/sq. These experiments were not successful as they resulted in very high sheet resistance values for automatic Resmap. The best way to move forward was to do ion implantation on the two process wafers. With 200 Ω/sq as a target for sheet resistance R_s, a dose of 5e14 $cm^{-3}$of boron at 50 KeV was used. This was followed by activation of the dopants in BTU2 with Recipe 354. The wafers were then dipped in BOE until they pulled out dry. The Resmap gave a sheet resistance value of ~1000 Ω/sq. The below Figure 27 shows a process wafer after being diced with the wafer saw.

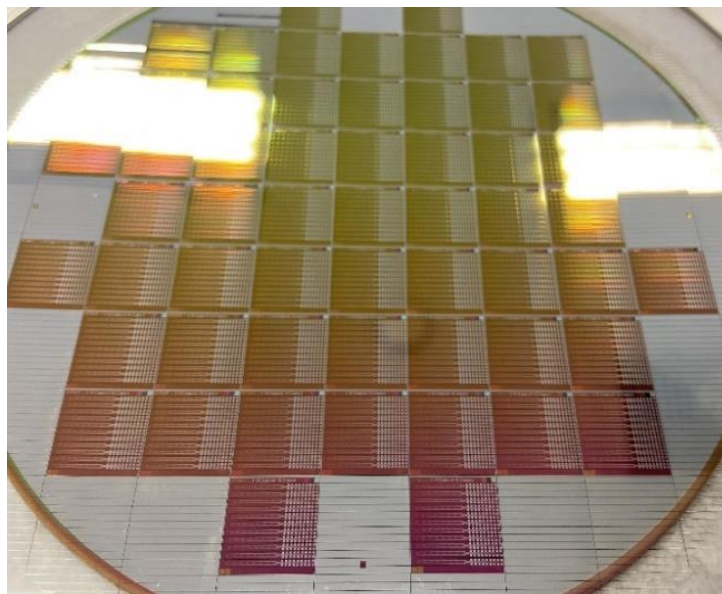

Figure 28. Process G1L2 wafer post wafer-saw

4.2.2 Preliminary Testing

During preliminary testing of the G1L2 sensors, it was discovered that the most recent lot of sensors had issues with the Polysilicon line-resistors being etched away during the XeF2 cavity etch as shown in Figure 28. These resistors are used to bridge the V1 & V2 signals underneath the Vdd, GND and aluminum traces of other sensors.

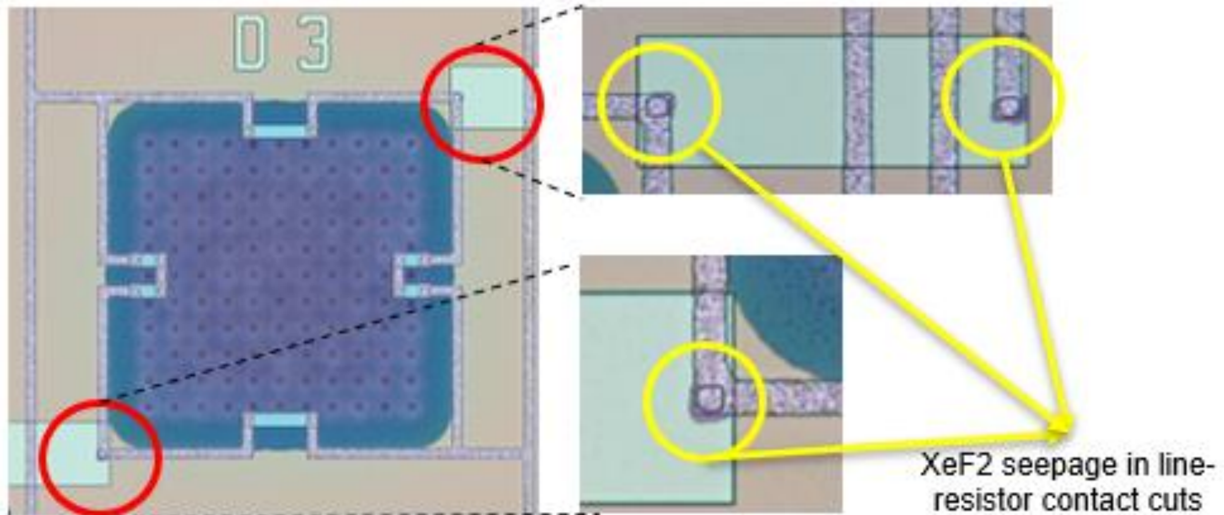

Figure 29. Poly line-resistor etching issue

Inspecting the sensors under the Scanning Electron Microscope revealed an extremely nodular aluminum deposition shown in Figure 29, which may have also contributed to the XeF_2 seepage into the resistors.

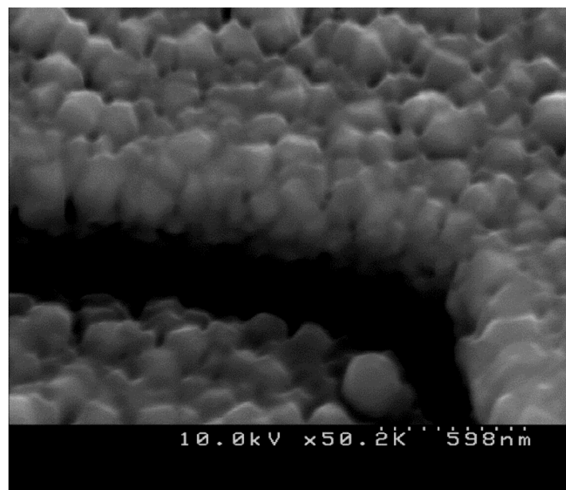

Figure 30. SEM showing insufficient overlap of Al over the contact cuts

The aluminum is not fully overlapping the contact cuts through the insulating nitride layer resulting in the polysilicon being eaten away and causing voltage output of the diaphragms to be floating. This is due to unsatisfactory overlap of the aluminum layer in layout, slight over etch of the aluminum or a combination of both.

The above line-resistor etching issue was addressed by carefully flowing epoxy over the contact cuts and completely covering them as shown in Figure 30. Care was also taken to avoid applying the epoxy to the side of the sensor array so that it can perfectly fit in the groove of the PCB during packaging. Delicate and precise application of the epoxy over the contacts was done using a fine probe needle tip. The epoxy is then left to air dry.

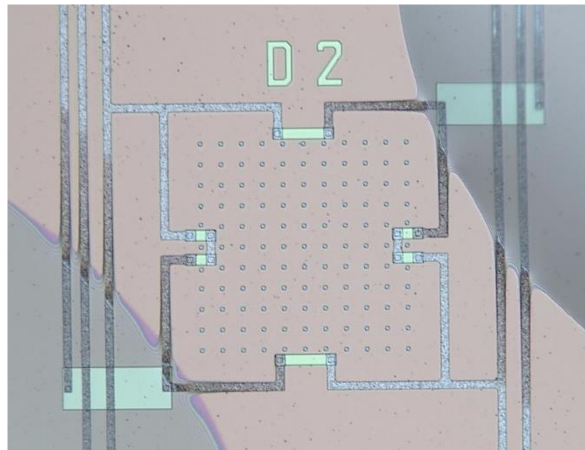

Figure 31. Epoxy cover before XeF2

Further, the sensors are etched into the XeF2 with cycles ranging from 15 followed by inspection, to check if the diaphragm is released or not, and then another required number of cycles. So far, a batch of 6 sensor arrays has been successfully etched for 25 cycles in the XeF2 tool. The epoxy covering the line-resistor contact pads has avoided the issue of polysilicon resistors being etched away. Below Figures 31 and 32 show the epoxy cover on a sensor and an array after the XeF_2 etch.

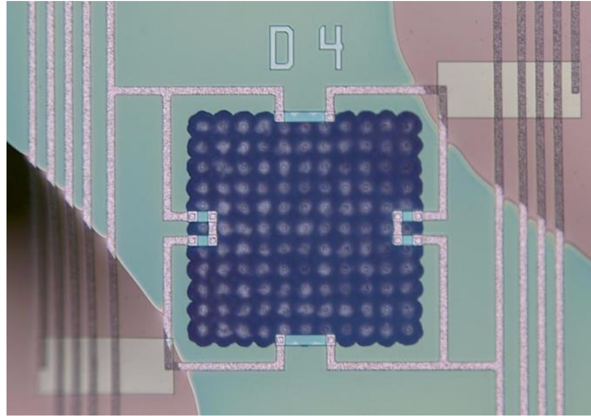

Figure 32. Epoxy cover after XeF2 etch

Figure 33. Sensor array with epoxy covering line-resistor contacts

5.0 Results

5.1 Resistance Testing

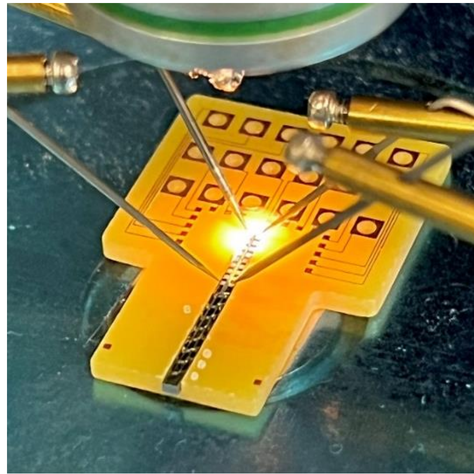

Figure 34. Probe station connections

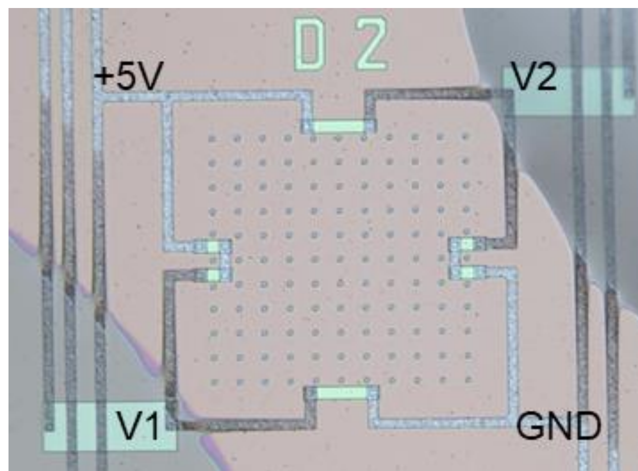

Figure 35. Probe connections on diaphragm

The resistances were measure on two full arrays before and after the XeF2 etch using a probe station shown in Figure 33. Two probes were touched down on pads on the sensor array assigned for +5V and GND. The other two probes were landed on V1 and V2 of each diaphragm as shown in Figure 34. A multimeter was used to measure resistances across any two points. The below Table 3 shows the average values measured on two devices.

Probe	Resistance
+5 to V1	9.2768 kΩ
+5 to V2	9.4817 kΩ
V1 to V2	17.919 kΩ
V1 to GND	9.3503 kΩ
V2 to GND	9.1978 kΩ

Table 3. Resistances corresponding to probe connections

Ideally, all the resistors in the Wheatstone bridge should be of the same value. But, as seen from the above table, the resistance values are not quite symmetric. This can be caused by improper alignment, resistor dimension mismatch, non-uniform doping and/or over etching of polysilicon. As all the diaphragms on an array have the same +5V and GND connection, it is difficult to measure the resistance of each individual Wheatstone bridge.

5.2 Voltage testing before XeF_2 etch

Before etching the devices in the Xatix XeF_2 tool, they were tested with +5V and GND applied to the bridge. The values observed on two different diaphragms of one particular sensor are shown in below tables 4 and 5.

Diaphragm 6	Probe	Voltage
	+5 to V1	2.5330 V
	+5 to V2	3.1320 V
	V1 to V2	**0.655 V**
	V1 to GND	2.5117 V
	V2 to GND	1.5333 V

Table 4. Diaphragm 6 Vout w.r.t probe connections

Diaphragm 7	Probe	Voltage
	+5 to V1	2.1435 V
	+5 to V2	2.9311 V
	V1 to V2	**0.733 V**
	V1 to GND	2.775 V
	V2 to GND	2.1063 V

Table 5. Diaphragm 7 Vout w.r.t probe connections

Ideally, the voltage across +5 to V1, +5 to V2, V1 to GND and V2 to GND should be 2.5V as they are in a voltage divider circuit. But, as the resistance values are not matching, there is some offset voltage observed across points V1 and V2 as seen from the above tables. These voltage values are consistent across devices.

5.3 Voltage testing after XeF_2 etch

Six sensor arrays with epoxy covering the polysilicon line-resistor contacts were etched in XeF2. These six arrays A1, A2, A3, A4, A5, A6 were etched together for total 25 cycles with time/cycle of 60 secs with XeF_2 at 3 Torr and N_2 at 2.2 Torr. When no pressure was applied, the voltage output response of the sensors was similar to that of the sensors before XeF_2 etch.

Diaphragm 1	**Vout (No Pressure)**
+5 to V1	2.5537 V
+5 to V2	2.7765 V
V1 to V2	**0.2229 V**
V1 to GND	2.4741 V
V2 to GND	2.2515 V

Table 6. No pressure Vout

An offset voltage of 0.22V was recorded across V1 and V2 as mentioned in above Table 6. The epoxy used to cover the polysilicon line-resistor contacts avoided the etching of line-resistors due to XeF_2. Various attempts were made to get a voltage output in response to applied pressure as mentioned below.

Attempt 1: Using a typical grain of salt

The pressure exerted by a known mass on a diaphragm of area A= 200 µm x 200 µm can be calculated by using the equation

$$P = F/A$$

where F is the force applied. The force applied by any object of mass m is given by

$$F = m * g$$

where g = 9.8 m/s^2 is the acceleration due to gravity. The operating pressure range of the sensors for this project is from 20 Pa to 1 kPa. Substituting the values in the above equations, and calculating mass required for given pressure, we get the values as shown in Table 7.

Pressure	Mass required
20 Pa	81.5 µg
1 kPa	4 mg

Table 7. Mass required for given pressure

The below Figure 35 shows a typical grain of salt of length 300µm resting on top of the 200µm diaphragm.

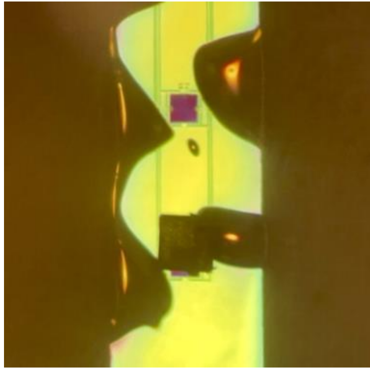

Figure 36. Typical grain of salt placed on a diaphragm

Salt (NaCl) has a cubic crystal structure. This salt grain did not cause any deflection of the diaphragm as its area was bigger than that of the square diaphragm. A smaller grain of salt with area less than the diaphragm area would be needed. A fifth probe micromanipulator was used to move these particles.

<u>Attempt 2</u>: Using the smallest grain of salt

Out of all the table salt grains, the smallest possible grain of salt that could fit on top of the diaphragm was found. This salt grain had almost the same area as that of our diaphragm shown in Figure 36.

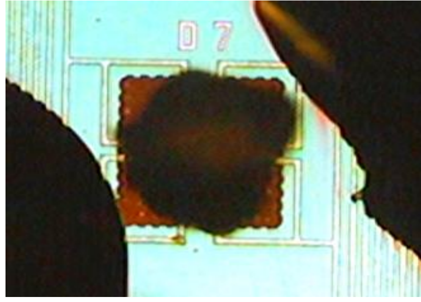

Figure 37. Smallest grain of salt placed on a diaphragm

The density of salt is ρ = 2.165 g/cm^3. Mass is the product of density ρ and volume V. The mass of a cubic grain of salt of side 200 µm was determined to be 17.32 µg. Hence, a salt grain is not heavy enough to test the sensors at their minimum operating range as it would not exert the minimum pressure required. As expected, an output voltage response was not observed.

Attempt 3: Metal ball

A metal ball of diameter 330 µm and density higher than that of salt was tried. It's calculated mass was 1.2 mg which was enough to exert the minimum required pressure. The metal ball on top of the diaphragm can be seen in the below Figure 37.

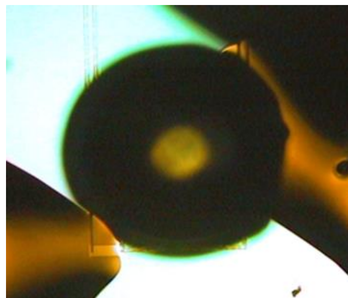

Figure 38. Metal ball placed on a diaphragm

The metal ball was affected too much by static and it would stick to the probe which was used to move it around. Even after placing the ball on top of the diaphragm, the output voltage was fluctuating a lot and sometimes floating, which could have been a result of shorting of metal lines.

Attempt 4: Probe pushdown

The fifth probe micromanipulator, which was being used to move around and place particles on top of the diaphragm, was then directly used two pushed down on the diaphragm as shown in Figure 38.

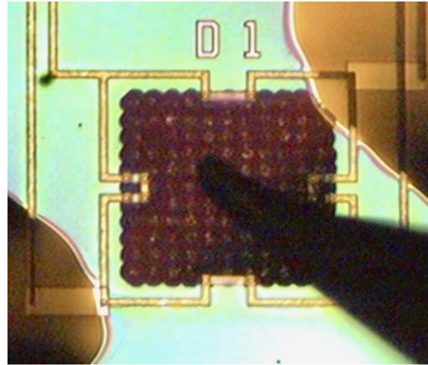

Figure 39. Probe tip pushdown on diaphragm

The voltage output was measured across the two points V2 and V1 on the Wheatstone bridge. This method was previously tried but resulted in a lot of ruptured diaphragms as even a $1/8^{th}$ turn of the knob, which is used to move the probe tip up and down, was too much deflection for the diaphragm. Also, the deflection of the diaphragm could not be observed under the probe station microscope as it was previously observed in G1L1 devices. If we could see any deflection, then that would have been a good reference point to start rotating the knob.

After all the failed attempts to get some output response, we reverted to the probe pushdown method again. This time the up/down knob was very slightly turned, and the voltage output was carefully observed as the probe tip reached the diaphragm. The voltage output was constantly monitored with the slightest of turns as the probe tip reached and touched the diaphragm. Finally, upon the slightest rotation of the knob, an increase in output voltage with respect to the offset voltage was observed. This point was marked as an initial reference point on the probe micromanipulator, seen in Figure 39. Further slight rotation increments resulted in further increase in the output voltage depicted in Figure 40. The results for the experiment are shown in the below Table 8.

Sensor A3 D1	No Pressure	Probe pushdown
+5 to V1	3.1410 V	-
+5 to V2	2.5275 V	-
V1 to V2	**0.6069 V**	**0.6159 V**
V1 to GND	1.8575 V	-
V2 to GND	2.4715 V	-

Table 8. Output voltage observed across V1 and V2 with probe pushdown

Pushdown	V1 to V2	Normalized Vout
0	0.6069 V	0.000 V
1	0.6159 V	0.009 V
2	0.6250 V	0.018 V
3	0.6406 V	0.033 V
4	Broke while handling	-

Table 9. Output voltage change with further probe pushdowns

For the sensor A3 D1, when no pressure was applied, the offset voltage across V1 and V2 was 0.6069 V. With the first probe pushdown, the Vout changed to from 0.669 V to 0.6159 V. This was an increment of 9 mV.

Figure 40. Probe knob rotation w.r.t a reference point

Figure 41. Change in output voltage observed

Upon further probe pushdowns, the Vout increased as shown in the above Table 9. The diaphragm then broke due to handling of the probe station. In this method, the degree of rotation of the knob was not measured. It was just eyeballed to keep the degree of rotation constant. The probe micromanipulator was then calibrated using the following two methods.

Displacement and Pressure Calibration 1: Using probe weight

A micro scale was used to measure the weight due to the probe tip pushdown. A 1/8th turn of the up/down knob gave a reading of 1.03 g which when normalized per turn gives 8.24 g/turn. This corresponds to a weight of 22.8 mg/degree or 2.28E-05 kg/degree. This weight value in kg was divided by the area of the diaphragm to give the expected pressure values. Expected pressure for a 1^0 turn was calculated to be 570 Pa. Displacement of the probe tip was then calculated using the equation for Ymax. Calculated displacement for a 1^0 turn was 2.8 µm.

Displacement and Pressure Calibration 2: Using probe displacement

A method of reliably measuring the rotation by equal degrees was needed. A digital version of a protractor was printed on a paper and glued to a cardboard. The degrees were then compared with a real protractor and verified to be exact. This was then taped just below the knob, with the center of rotation of the knob matched with the midpoint of the protractor as shown in below Figure 41. A metal wire was taped on top of the knob and bent downward to mark angles on the protractor.

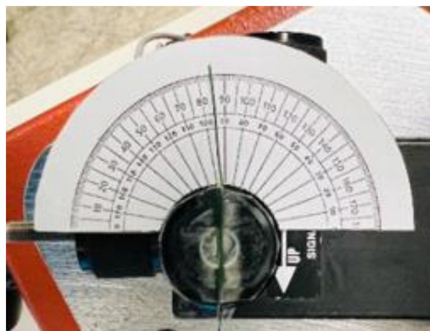

Figure 42. Marking angles on protractor by rotating probe knob

The displacement of the end of probe tip with a full 360^0 turn was 1 mm which was measured with a vernier caliper set besides it. This gives a displacement of 2.77 µm/degree or 2.77E-06 m/degree. The expected pressure was then calculated using the equation for Ymax. Expected pressure for a 1^0 turn was calculated to be 564.24 Pa.

The displacement and pressure values for every degree turn of the knob were close for both the calibration methods. A graph was plotted for the displacement of every degree turn for both calibrations as shown in below Figure 42. The displacement and pressure exerted by the probe pushdown method was successfully calibrated and further used for getting output voltage responses of sensor arrays.

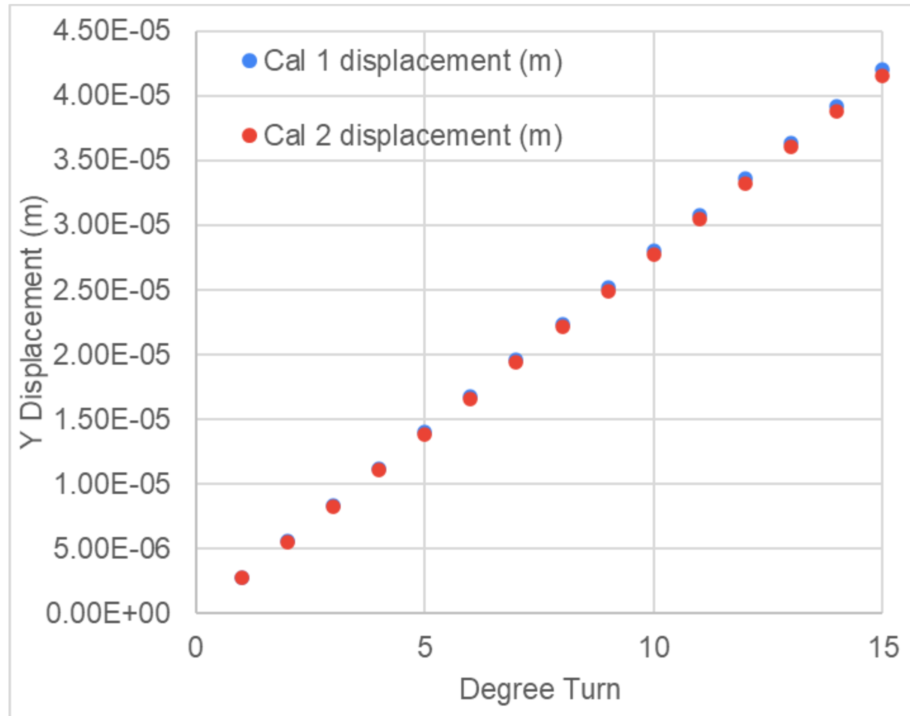

Figure 43. Graph for displacement of every degree turn for both calibrations

<u>Deflection study</u>: The pressure is applied on top of the diaphragm via the probe pushdown method. The deflection at the center of the diaphragm for the specified pressure range (20 Pa– 1 kPa) thus obtained are plotted as shown in below Fig. 43. It is obvious from the deflection results that the maximum deflection at 1 kPa is 5.6 µm. The deflection curve shows that better linearity is ensured in this structure.

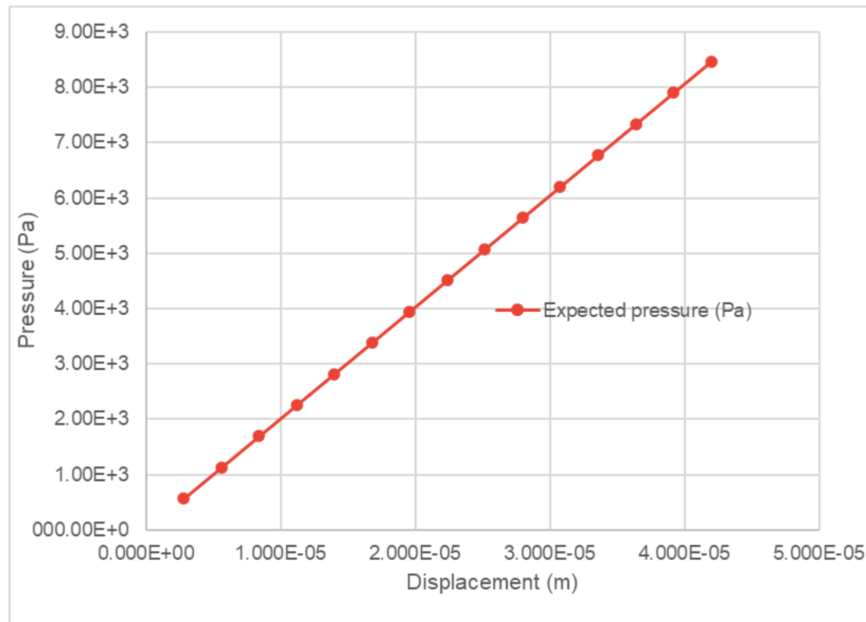

Figure 44. Graph for deflection w.r.t pressure applied

The voltage outputs were recorded for three different sensors S1, S2 and S3 by applying pressure using the probe pushdown method. With every degree turn, the normalized Vout values are displayed in the following Table 10 and compared to our target Vout values.

Degree Turn	S1 Vout	S2 Vout	S3 Vout	Target Vout
1	0.003	0.002	0.002	0.003
2	0.005	0.004	0.007	0.006
3	0.007	0.006	0.013	0.009
4	0.009	Ruptured	0.022	0.011
5	0.011		0.028	0.014
6	0.014		0.037	0.017
7	0.017		0.044	0.020
8	Ruptured		0.050	0.023
9			0.055	0.026
10			0.060	0.029
11			0.066	0.031

Table 10. Normalized Vout of S1, S2, S3 compared to target Vout

The sensor output is recorded as the pressure is varied from turning the knob of the probe micromanipulator by 1 to 11 degree rotation. Figure 44 shows the voltage output of the sensors as a function of degree turn.

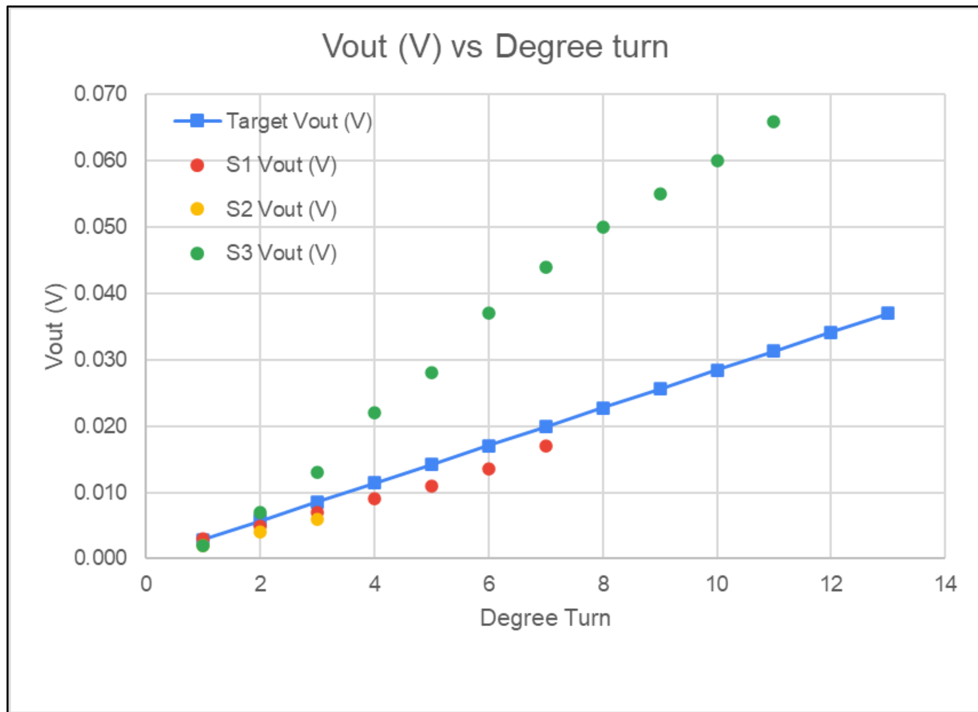

Figure 45. Graph for Vout vs Degree Turn

The sensor output is recorded as the pressure is varied from 570 Pa to 6300 Pa (1 to 13 degree rotation). Figure 45 shows the voltage output of the sensors as a function of the pressure on the diaphragm.

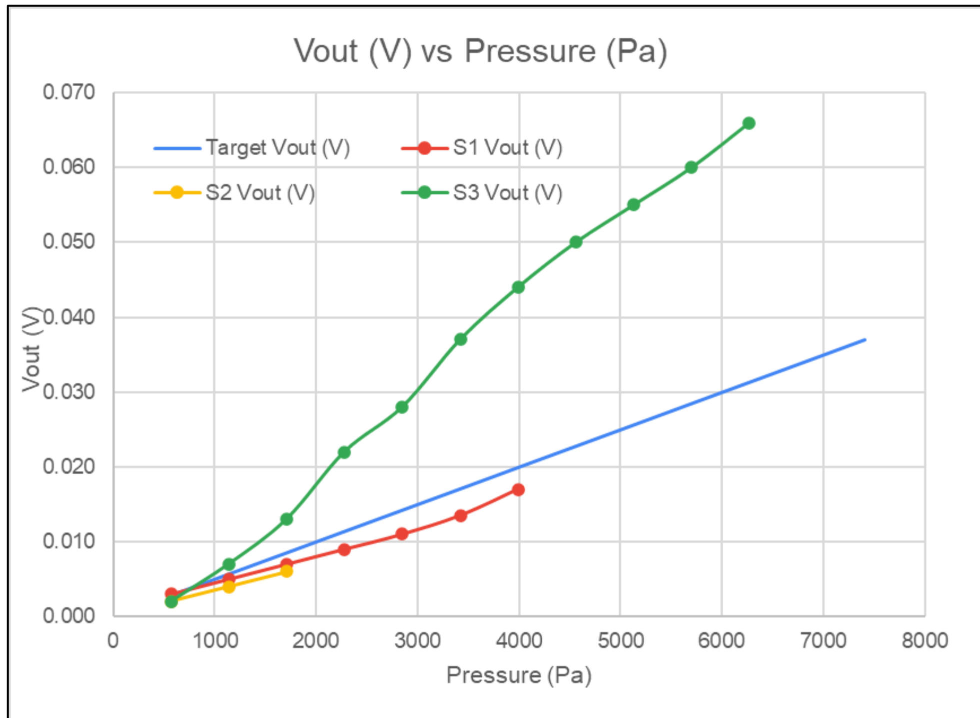

Figure 46. Graph for Vout vs Pressure

These values are acquired over a number of experiments repeated at similar experimental conditions to demonstrate the repeatability of the calibration data. The value of sensitivity for sensor S1 as derived from the slope of the linear calibration plot shown in Figure 45 is 5.26 µV/Pa which is very close to our target sensitivity of 5 µV/Pa.

Gauge Factor: The gauge factor for the polysilicon strain gauges can be estimated by using the experimental Vout, pressure and displacement numbers. For sensor S1, the output voltage Vout is 0.003 V for a pressure of 570 Pa. The corresponding stress on the diaphragm of length L of 200 µm and thickness H of 0.225 µm is given by the Equation (4).

$$\sigma = (0.3)\left(\frac{L}{H}\right)^2 * P = 135 \text{ x } 10^6 \text{ N}/m^2$$

Knowing the stress, strain can be derived from the relationship mentioned in Equation (5). E is the Young's modulus which is 140 GPa for lightly doped polysilicon resistors.

$$\varepsilon = 9.65 \text{ x } 10^{-4}$$

Resistance of every resistors of L= 50 µm, W= 10 µm, and Resmap R_s of 1000 Ω/sq is calculated to be R_0 = 5000 Ω from Equation (6).

The resistance of parallel resistors R1 and R4 decreases as their width increases due to strain. The change in width W^1 is given by

$$W' = W + (W * \varepsilon) = 10.009 \text{ µm}$$

Therefore, by substituting above W' in Equation (6), the resistance of R1 and R4 changes to

$R_{(\varepsilon)}$ = 4995.179 Ω.

The resistance of perpendicular resistors R2 and R4 increases as their length increases due to strain. The change in length L^1 is given by

$$L' = L + (L * \varepsilon) = 50.048 \text{ µm}$$

Therefore, by substituting above L' in Equation (6), the resistance of R2 and R3 changes to

$R_{(\varepsilon)}$ = 5004.825 Ω.

The Gauge factor can then be determined by using the Equation (3) as shown:

$$G = \frac{(R_{(\varepsilon)} - R_0)/R_0}{\varepsilon}$$

Where, $R_{(\varepsilon)}$ is the resistance of strain gauge at strain ε and R_0 is the resistance of strain gauge at zero strain. The Gauge factor in longitudinal direction for resistors R2 and R3 is calculated to be $GF_L = 1$ and in the transverse direction for resistors R1 and R4 is $GF_T = -0.99911$.

6.0 Packaging

There are many ways to implement packaging methods to a die added to a printed circuit board (PCB). But the one used in this project is the die level packaging. It is a similar process to those found in the IC industry by combining IC and MEMS together in one.

6.1 PCB Design

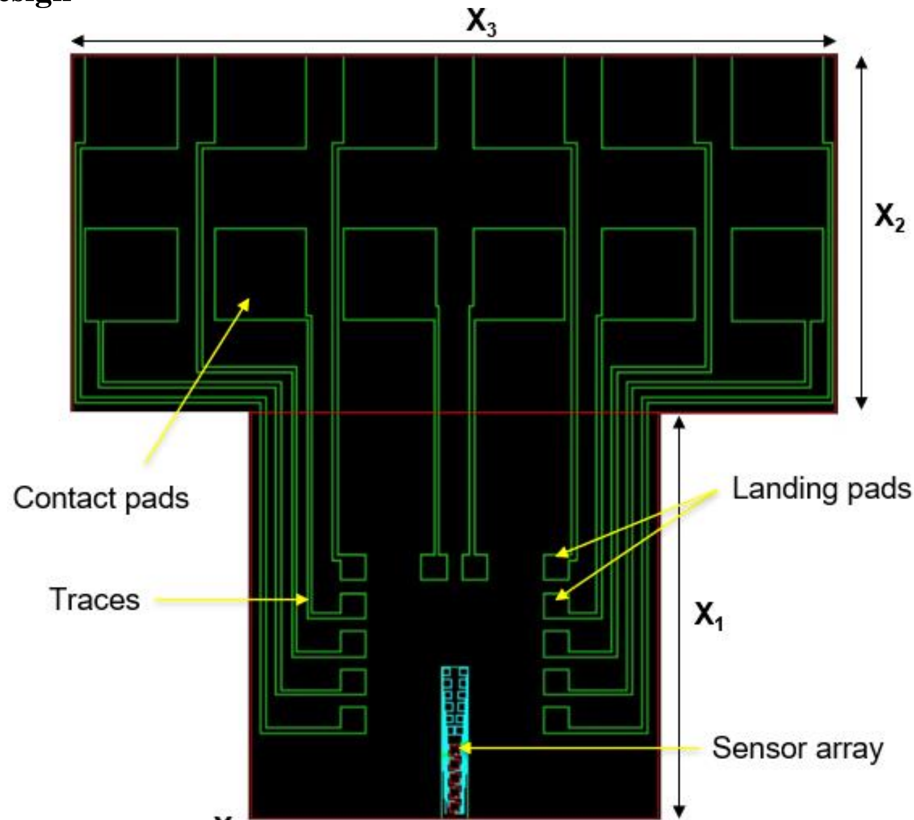

Figure 47. G1L1 PCB layout

G1L1 design: A custom PCB design was created for this project using Mentor Graphics Pyxis software as shown in Figure 46. The PCB design has a pitch of 0.1 inch for the contact pads so that the male connectors can be inserted through them. The landing pads are to be wire bonded directly to the aluminum pads on the sensors. This PCB design has 12 contact pads and 12 landing pads. The G1L1 sensor array has 5 diaphragms with a common Vdd and GND connection. Further, each diaphragm has two outputs V1 and V2 and hence there are total 12 aluminum pads on each sensor array. The contact pad area in the top half of the PCB is 1800µm by 1800µm and the landing pad area in the bottom half

is 500µm by 500µm. The copper traces are 100µm wide. As seen in figure __, the PCB is 15 mm wide (X_3) on top, with a total height of 15mm (X_1 +X_2). The bottom square part of the PCB is 8mm by 8mm (X_1*X_1) so that it can be perfectly mounted at the end of the tapered rod in the setup.

G1L2 design: The G1L2 PCB design consists of six additional contact and landing pads respectively due to the addition of three more diaphragms in the sensor array. The contact and landing pad area as well as the trace width is the same as G1L1 design.

6.2 PCB Mask Layout

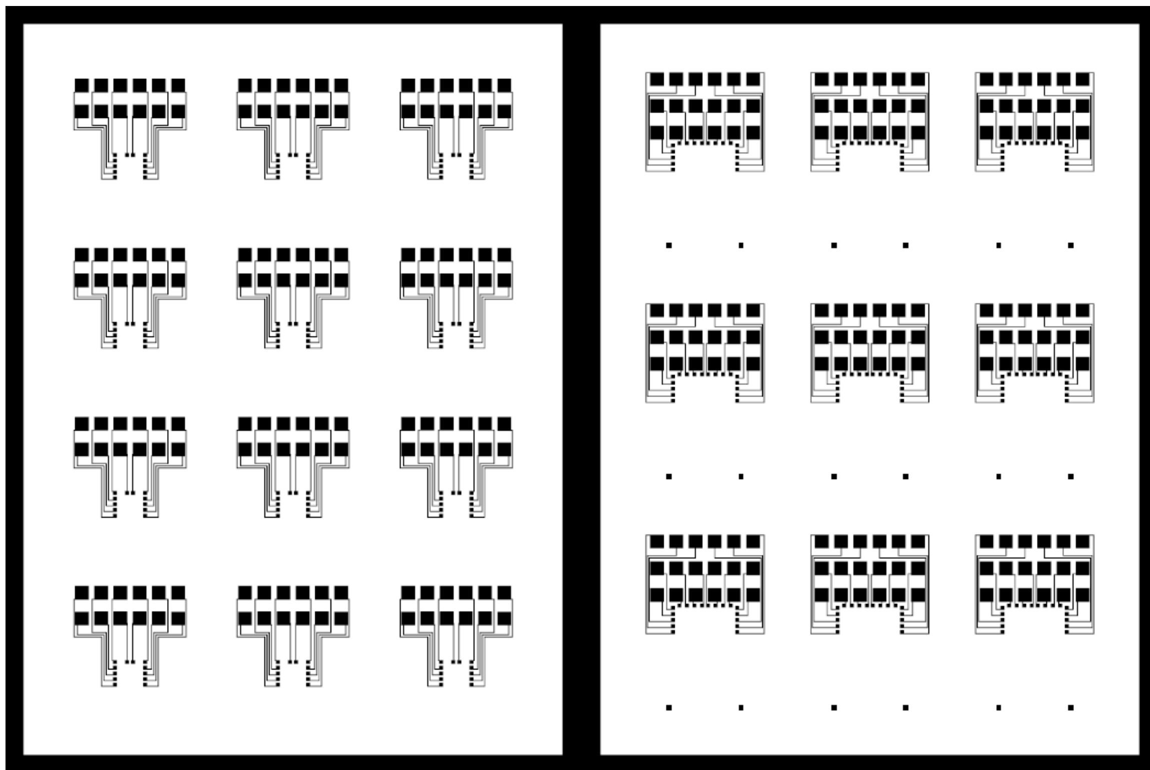

Figure 48. 4x6" CAD layout of PCB mask consisting of G1L1 (left) and G1L2 (right) designs

A CAD file for a 4x6-inch mask was created consisting both designs as shown in above Figure 47. The mylar mask with a plot resolution of 20K dpi and minimum feature size of 15 microns was ordered from Fine Line Imaging, Colorado.

6.3 PCB Fabrication at SMFL

Single-sided copper board was used for the in-house fabrication of the PCBs using the mylar mask. First, cleaning the copper boards with sandpaper, followed by using fine steel wool. This cleans the board and the copper from any impurities. At the same time, it removes the oxidized or aged copper from the mixture of air particles. Further, the boards are washed using soap water and then blow-dried.

Photoresist HPR504 was then spin-coated at 1500 RPM for 16 seconds. This is followed by baking the PCBs in the oven at 100°C for four minutes. The transparent mylar mask was then placed on top of the copper boards and flattened with a glass plate. The whole setup was flood exposed for 20 seconds at 100 millijoules per centimeter square using the Karl Suss MA150. After exposure, the PCBs were developed in CD-26 developer for one minute and inspected. The boards were then rinsed with water followed by a hard bake in the oven at 140°C for 15 mins. The copper was then etched in a mixture of water H2O2 and HCL at a ratio of 3:2:1. The photoresist was stripped in acetone, followed by rinsing of the boards with water and blow-drying.

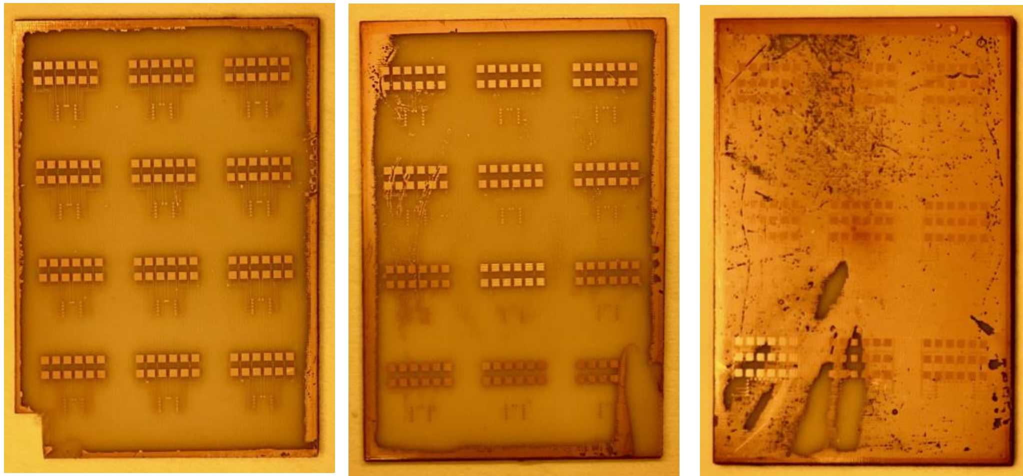

Figure 49. Copper boards after wet Cu etch

Upon final inspection, on only one out of the three boards, the copper was etched successfully as seen in the above Figure 48. The copper traces were not fully released, and copper residue was left behind which resulted in shorting of the lines. This could be because the photoresist that was used was

expired. Hence, we decided not to pursue this method of fabricating the PCBs in-house.

6.4 Final Packaged Sensors

The PCBs were manufactured via a third party. Ten boards were successfully printed as shown in Figure 49 and shipped back.

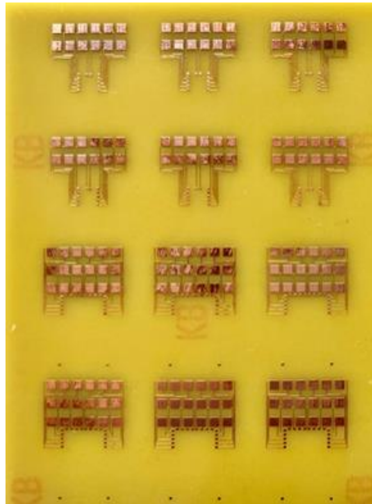

Figure 50. PCBs ordered via pcbway

These new printed circuit boards were initially manually cut using a rotating Dremel tool setup in the test lab. The tiniest drill bit of 0.4 inches was used to drill holes into the contact pads. This manual cutting and drilling of PCB using the Dremel tool resulted in a lot of PCB dust flying around, which could cause respiratory problems. PCB resin (aka FR4 - which is the most common) is fiberglass. Its dust most certainly is toxic and recommended not be inhaled. Also, this process was very hectic and time-consuming. Hence, an alternate method of using the CNC machine was implemented.

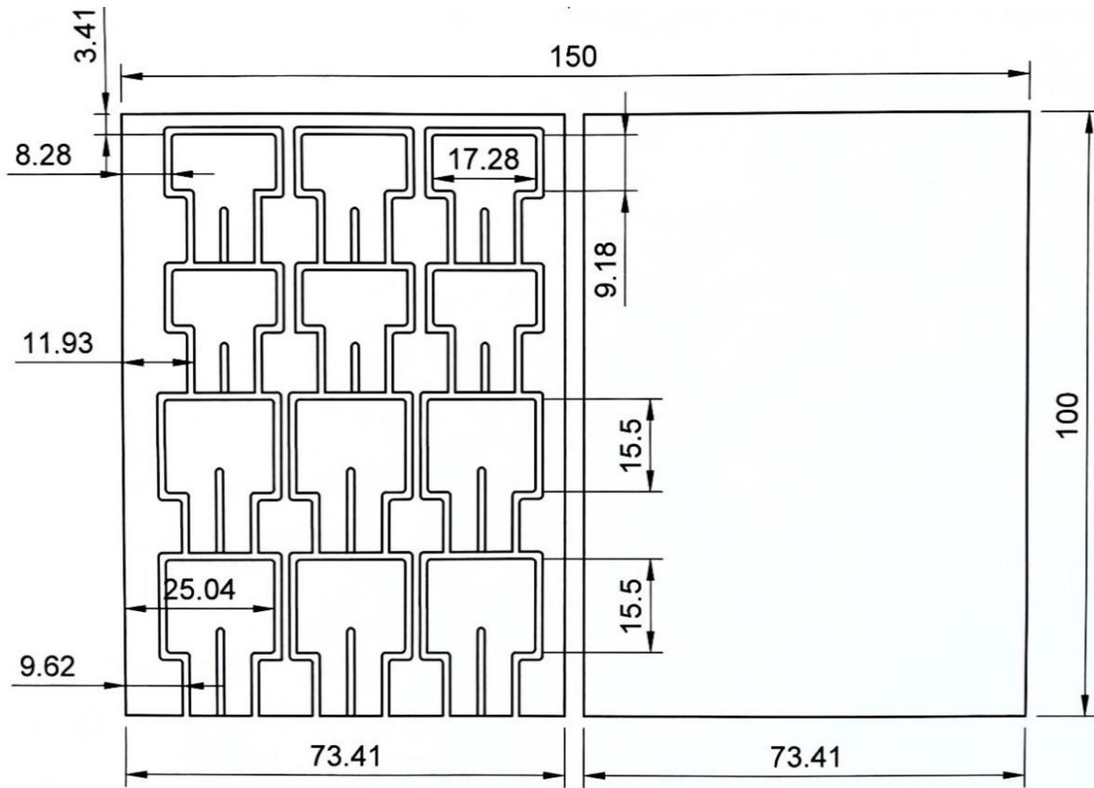

Figure 51. Fusion360 layout for CNC machine to cut individual PCBs

A CAD layout for the CNC machine was modeled using Fusion360, as shown in Figure 50 above. The layout consists of the end mill tracing the PCB designs on the outside. All dimensions for the layout are in millimeters and one mill diameter in tolerance was used. Holes were added to the layout so that the CNC machine could also drill the holes.

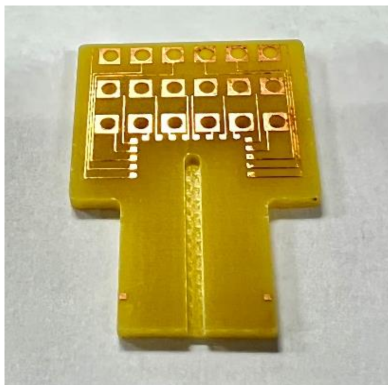

Figure 53. Individual PCBs after CNC milling and drilling

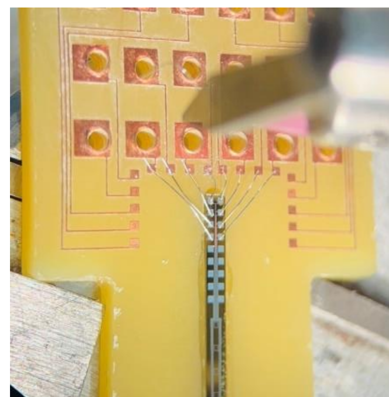

Figure 52. Wire bonding

A new mill bit of diameter 3/64 inch and drill bit of 1/32 inch was ordered. Both these are carbide tips to avoid wear out over time. The drill bit size was chosen so the male connector pin would seamlessly go through the hole. The mill bit diameter was particularly chosen so that the groove dimensions on top of the PCB match the sensor array dimensions. As a result, the sensor array will perfectly fit into the groove. The PCBs were double sticky taped on top of a wood surface and then put into the CNC machine for machining. The CNC machine gives an excellent cut, and the cuts are very precise as can be seen in Figure 52.

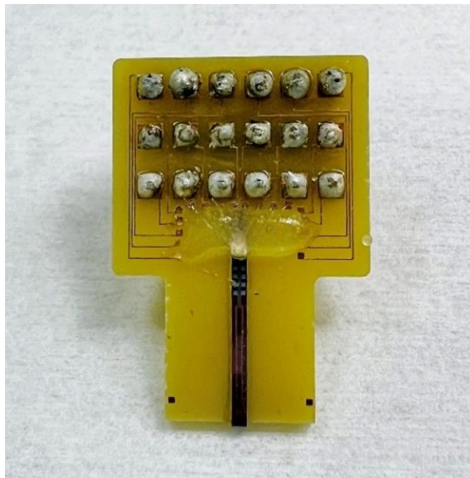

Figure 55. Front view of final packaged sensors

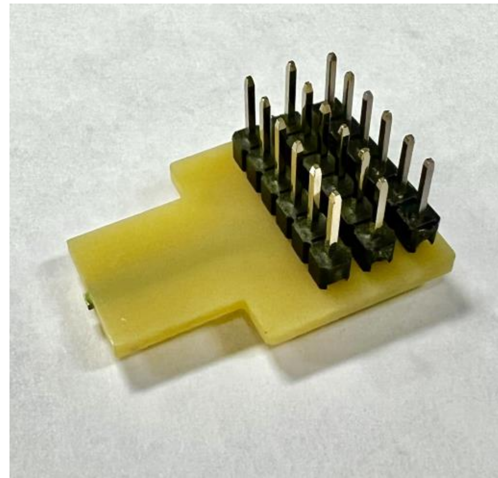

Figure 54. Back view of final packaged sensors

Epoxy is then applied into the groove of the PCB, and the sensor is carefully placed into it. This is followed by wire bonding the sensor to the PCB as shown in Figure 51. The contact pads on the sensor are carefully wire bonded to the copper landing pads on top of the PCB. Epoxy is then applied on top of the wire bonds to keep them in place, followed by curing the epoxy at room temperature. The male connectors are then inserted into the holes drilled in the PCB. Male header pins are then soldered using a high heat solder (Figures 53 and 54). Female to male wires are then attached to the male header pins, and the whole setup is checked for continuity. These fully packaged sensors will be provided to Dr. Kandlikar's students, and LabView will be used for data acquisition and analysis. Wet preliminary testing can then be carried out on these fully packaged sensors.

7.0 Setup Schematic

The following sections enunciate the design, assembly, and working of the setup.

7.1 Bubble Air-Injection Setup

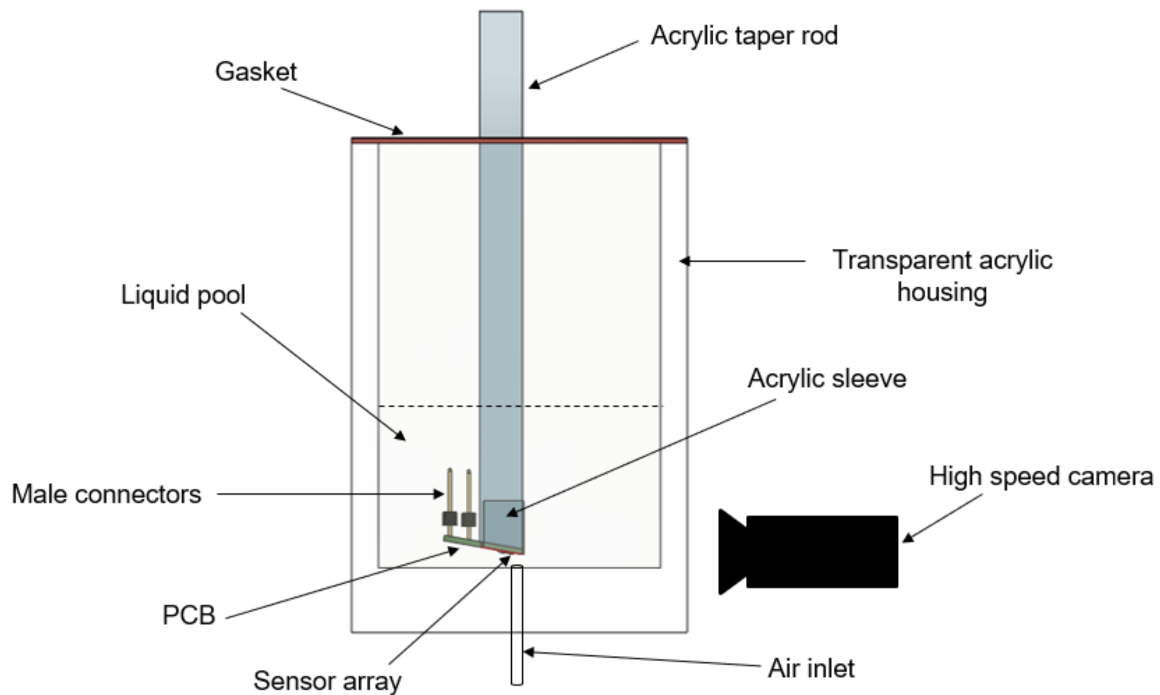

Figure 56. Wet test setup - Dielectric liquid

Figure 55 shows the schematic diagram of the air-injection assembly for testing in dielectric liquids. This wet testing setup includes a transparent acrylic housing with a dielectric liquid pool inside. The first generation of sensors will be tested in a dielectric liquid as they are not waterproofed. The G1L2 sensor array is epoxied inside a groove on the PCB. The sensors are then wire bonded to the PCB. Holes are drilled into the PCB for the male connectors which are then be soldered. The packaged sensors will be mounted at the end of an acrylic tapered rod. Bubbles will then be introduced through an air injection system which will hit the sensor array, squeeze, grow in size and travel along the length of the sensor array. This whole setup will be sealed using a silicone rubber gasket. A 3-D version of the dielectric setup schematic is shown in below Figure 56.

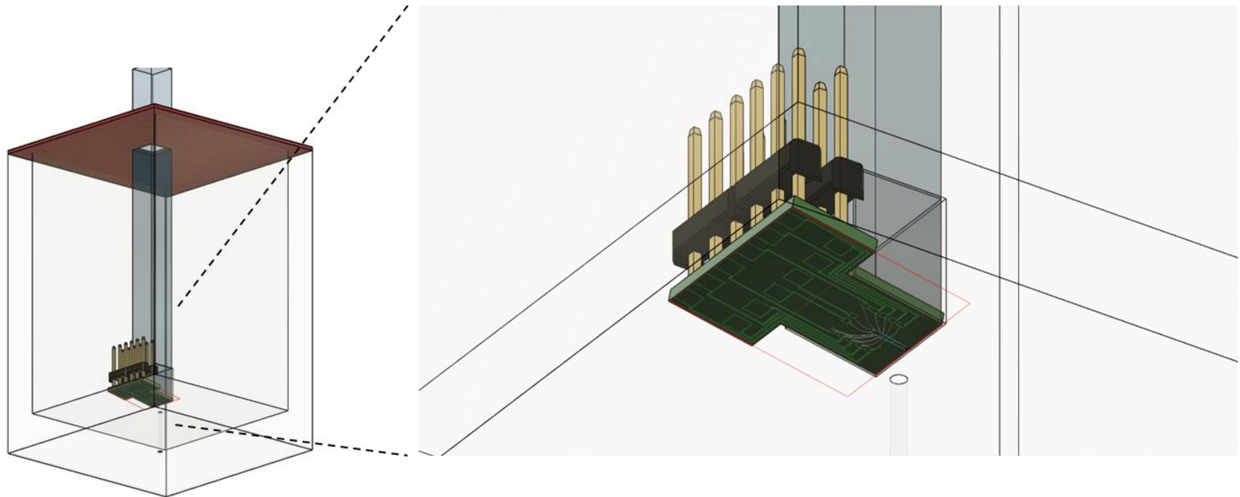

Figure 57. Bubble formation through air injection

7.2 Experimental Setup

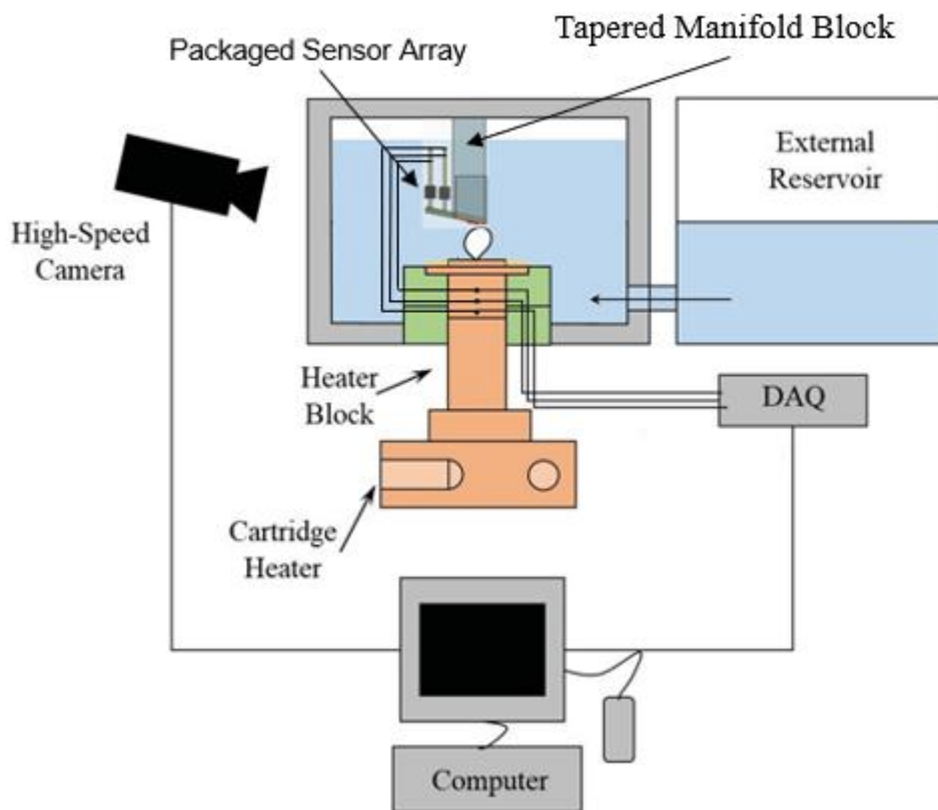

Figure 58. Boiling setup schematic

The experimental setup as shown in Fig. 57 is developed to study the pressure field around a squeezing bubble. The heated test surface will have a linear notch parallel to the inlet edge to promote nucleation at a fixed distance from the inlet to control the exact location of the bubble nucleation in the microgap. The tapered manifold block contains the packaged sensor array with predefined linear arrangement of piezoresistive pressure sensors mounted on the top cover. The pressure sensors will measure the pressure field around the bubble in the tapered microgap region. The bubble expansion in the tapered microgap will be visualized using a high-speed camera. The gap height is around 100 – 500 μm while the taper angle is between 1° and 4° for a heater surface length of 10 mm with water as the working fluid. The effect of taper angle and microgap height will be evaluated. The top surface of the manifold block is attached to two servo motors. Servo motors 1 and 2 will be used to adjust the gap height and the taper angle. Different working fluids such as water, HFE-7000 and ethanol will be tested. The experimental findings from this study will be compared with numerical simulations and theoretical model for respective validations. LabView will provide the software to monitor and record the data onto the computer.

8.0 Conclusion

The findings in this study have proven that hyper-sensitivity of 5 µV / Pa can be achieved in the MEMS based pressure sensors of diaphragm 200 µm x 200 µm, and 0.225 µm thick that will allow effective measurement of the pressure exerted (20 Pa to 1 kPa) by a nucleating bubble. The calculations and simulations seemed promising, and the design fits the application use. The sensor array can be used to measure pressure at various stages of bubble growth in a dielectric liquid pool. The findings indicated that the optimum design was obtained under the combined parameters of 0.225 µm diaphragm thickness, 1-turn meander shaped perpendicular piezoresistors, and 0-turn meander shaped parallel piezoresistors . It can be concluded that the sensitivity of the sensor was highly influenced by the diaphragm thickness, the shapes of the piezoresistors, and their placements on the diaphragm. The processing knowledge gained will be invaluable for future iterations of the sensor design to be used in conducting fluids.

9.0 Future Work

Based on the recent progress made on this project, future work on proceeding toward the end goal of producing accurate pressure sensors for bubble pressure measurement would require preparing a new layout and fixing the issues temporarily remediated by the epoxy application solution, and improving the functionality of sensors. Adjusting the sputter recipe in the upcoming device layout may be necessary to achieve a more uniform Al deposition. This is because, upon inspection of the sensors under the Scanning Electron Microscope, it revealed a very grainy aluminum deposition, which may have contributed to the XeF_2 seeping through the contact cuts into the poly line-resistors and etching them away. In the new device layout, a larger overlap of the aluminum pad over the line-resistor contact cuts would be required. Also, a possible investigation of different aluminum etch methods will be beneficial, as the wet etching technique used for aluminum resulted in some inconsistent etching.

An alternate solution would be substituting the polysilicon line-resistors with a second aluminum layer. Theoretically, the line resistance imposed by the polysilicon does not affect the measurement of voltage across the bridge due to the high internal impedance of the instruments. However, using aluminum could reduce the chance of device failure at the cost of increased processing time. These features could be copied from the poly layer of the layout to a new layer, or a new layer created from scratch with the same trace width as the previous aluminum layer.

Another thing to be considered in the revised layout is to prepare for testing in fluids, specifically conductive fluids like water. A conformal coating will be needed around the wires and aluminum traces along with waterproof connectors. A new layer can be added to the mask layout to coat the chips with Parylene C, which could act as a final passivation layer. Finally, an idealized

process flow can be produced for the sensors based on information gathered from the previous runs and determine if any of these process modifications are enough to benefit for future runs that will support the development of numerical models.

9.1 Proposed Surface Micromachining Process flow

A surface micromachined process can be used as an alternative to the bulk micromachined process. The SMM provides better dimensional control as it is not limited to a low aspect ratio in geometry. The CMOS integration is good as devices are built up from the wafer layer by layer. The diaphragm formed with the SMM process will not have holes for XeF_2 cavity etch as opposed to the BMM process. Also, the devices fabricated will have better mechanical properties. The proposed surface micromachining process flow is depicted in the below Figure 57, 58.

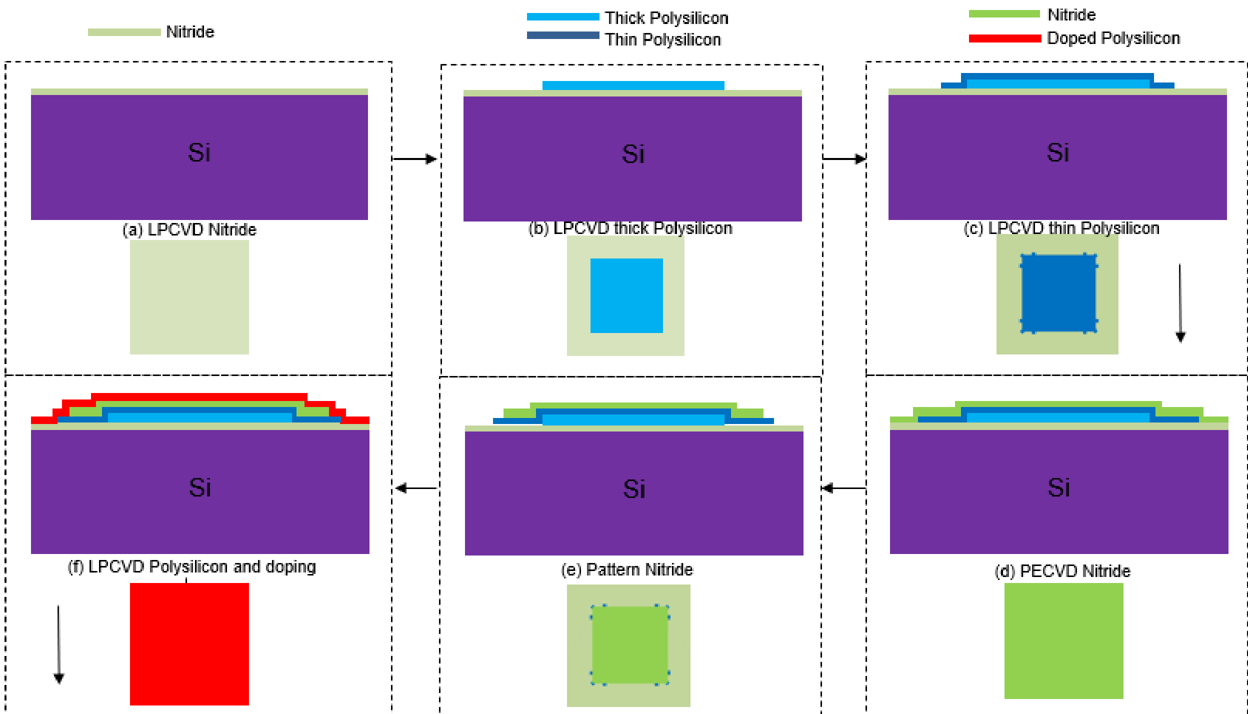

Figure 59. Proposed Surface Micromachining Process flow

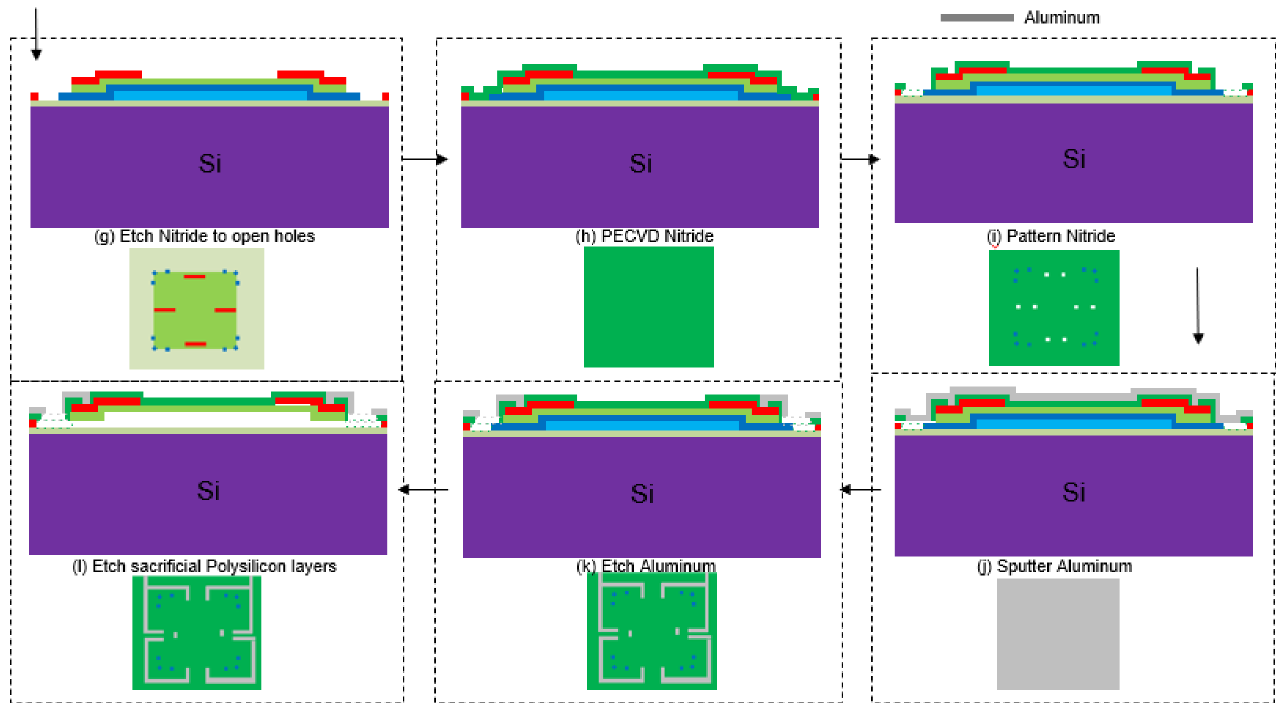

Figure 60. cont. Proposed Surface Micromachining Process flow

References

[1] Incropera, F. P., and DeWitt, D. P., 2002, Fundamentals of Heat and Mass Transfer, J. Wiley, New York.

[2] Nukiyama, S., 1966, “The Maximum and Minimum Values of the Heat Q Transmitted from Metal to Boiling Water under Atmospheric Pressure,” International Journal of Heat and Mass Transfer, 9(12), pp. 1419–1433.

[3] Maharshi Y. Shukla, Satish G. Kandlikar, “Influence of Liquid Height on Bubble Coalescence, Vapor Venting, Liquid Return, and Heat Transfer in Pool Boiling”, International Journal of Heat and Mass Transfer, Volume 173, 2021, 121261, ISSN 0017-9310, https://doi.org/10.1016/j.ijheatmasstransfer.2021.121261.

[4] “MEMS Pressure Sensors | The Design Engineer’s Guide | Avnet Abacus,” Avnet.com, 2018. https://www.avnet.com/wps/portal/abacus/solutions/technologies/sensors/pressure-sensors/core-technologies/mems/

[5] Kottapalli, Ajay GP, et al. "A flexible liquid crystal polymer MEMS pressure sensor array for fish-like underwater sensing." *Smart Materials and Structures* 21.11 (2012): 115030.

[6] Angel, S., and R. Joseph Daniel. "Sensitivity enhancement by striped arrow embossed diaphragms in low pressure MEMS piezoresistive pressure sensors." *2017 Trends in Industrial Measurement and Automation (TIMA)*. IEEE, 2017.

[7] C. Herring, E. Vogt, Transport and deformation-potential theory for many-valley semiconductors with anisotropic scattering, Phys. Rev. 101 (1956) 944–961.

[8] Y. Onuma, K. Sekiya, Piezoresistive properties of polycrystalline silicon thin film, Jpn. J. Appl. Phys. 11 (1972) 20–23.

[9] J.Y.W. Seto, Piezoresistive properties of polycrystalline silicon, J. Appl. Phys. 47 (1976) 4780–4783.

[10] V. Mosser, J. Suski, J. Goss, E. Obermeier, Piezoresistive pressure sensors based on polycrystalline silicon, Sens. Actuators, A 28 (1991) 113–132.

[11] E. Obermeier, P. Kopystynski, Polysilicon as a material for microsensor applications, Sens. Actuators, A 30 (1992) 149–155.

[12] S. H. Christie, “Experimental Determination of the Laws of Magneto-electric Induction in different masses of the same Metal, and of its Intensity in different Metals”, Phil. Trans. Roy. Society, vol. 123, pp 95-142, 1833

[13] C. Wheatstone, “An account of several new Instruments and Processes for determining the Constants of a Voltaic Circuit”, Philos. Trans. Roy. Soc. London, vol. 133, pp 303-324, 1843

[14] M. Mohamad, N. Soin and F. Ibrahim, "Design optimisation of high sensitivity MEMS piezoresistive intracranial pressure sensor using Taguchi approach," Microsystem Technologies : Sensors, Actuators, Systems Integration, vol. 24, (6), pp. 2637-2652, 2018.

[15] N. B. Vargaftik, et al., International tables of the surface tension of water, J. Phys. Chem. Ref. Data, 12, 817, 1983.

[16] Chauhan, Aranya, and Satish G. Kandlikar. "Geometrical effects on heat transfer mechanisms during pool boiling in Dual Tapered Microgap with HFE7000." *International Journal of Heat and Mass Transfer* 183 (2022): 122165.

[17] Chauhan, Aranya, and Satish G. Kandlikar. "Characterization of a dual taper thermosiphon loop for CPU cooling in data centers." *Applied Thermal Engineering* 146 (2019): 450-458.

Appendix

NSF Pressure Sensor Project
G1L1 BULK MICROMACHINED MEMS PROCESS FLOW

	Instructions	Review/Sign
1	Obtain qty. __, 6" n-type wafers Resmap: Rs = 45 Ω/sq ρ = 2.9 Ω·cm (Expected= 1-15 Ω·cm)	
2	RCA clean. **SC1** H20 – 5000 ml NH4OH – 300 ml H2O2 – 300 ml 75°C, 10 min DI water rinse: 5 min **HF**, 60 sec DI water rinse: 5 min **SC2** H20 – 5000 ml HCl – 300 ml H2O2 – 300 ml 75°C, 10 min DI water rinse: 5 min	
3	Photo level 0: alignment marks Coat wafer Resist MiR701 (SVG2 track): Recipe: Program 4 - No EBR Expose using ASML Stepper Stepper job: TAYLOR Stepper Mask: Level 0 Combi reticle Develop in wafer track. CD-26 Program 1	
4	Etch Alignment Marks (Resist burned in RIE Etch Trion) Plasma etch in LAM 490 Recipe: FACTORY > ZERO.RCP Inspect resolution	
5	Solvent Strip: PRS 2000	
6	RCA clean standard	
7	Grow 1000Å Oxide: Dry Oxide tube Recipe: 462 Nanospec: 1011Å	

8	Deposit 4500Å Polysilicon LPCVD Recipe 610 poly Soak time from log sheet = 50min was >4500A on 3/5/21 Soak time = 50 min Enter Nanospec thickness: C12 1: 4557, 2: 4579, 3: 4585, 4: 4560, 5: 4550, 6: 8093, 7: 10310, 8: 9124, 9: 8109	
9	Spin-on Dopant Borofilm 150, include dummy 3000 rpm 30sec 1s ramp Blue oven bake at 200C for 20 minutes in air ambient	
10	Dopant Diffusion Bruce Furnace Tube2 Recipe: 354 15min N2 ramp to 1050C 5min N2 soak at 1050C 5min wet O2 soak at 1050C 15min N2 ramp down	
11	Etch SOG and Masking Oxide ~10 min (10:1) BOE until wafers pull dry Wafer should look clean, like bare Silicon. Nanospec <100Å	
12	Four Point Probe Dummy Wafer (manual or RESMAP) Rs should be around 100 Ω/sq Resmap Rs: 200 Ω/sq ρ = _____ Ω·cm (Target ~.009Ω·cm)	
13	Photo 1: Poly Coat in SVG2 track. Recipe 4 - No EBR Expose using ASML Stepper Stepper job: PUCHADES_PRESS Stepper mask: L1 "POLY" Energy: __275 mJ/cm2____ Develop in wafer track. CD-26 Recipe: Default Enter minimum resolution line: ______ um	

14	Etch poly, LAM490 Recipe: FACPOLY4K.RCP Endpoint detection may not work. (Expect ~1'05'') SF6: 150 Time/wafer = 1min 15 sec	
15	Strip Resist 5+5 min PRS2000 solvent clean + 5 min DI water rinse + SRD	
16	RCA Clean Only 20sec in HF due to exposed oxide.	
17	Oxidize Poly Recipe 354 15min N2 ramp to 1050C 5min N2 soak at 1050C 5min wet O2 soak at 1050C 15min N2 ramp down Enter Nanospec thickness: 1_____, 2______, 3_______, 4______, 5______	
18	Deposit 3000 Å Nitride Tube 2 LPCVD Recipe: Low stress Nitride Soak time from log sheet = 80 min was 470 nm in 2018 Soak time: 90 min Enter Nanospec thickness: 3311Å – 5449Å	
19	Photo Level 2: Nitride Contacts Coat in SVG2. Recipe 4 no EBR Expose using ASML Stepper Stepper job: PUCHADES_PRESS Stepper mask: L2 "CONTACT_CUTS" Energy: 275mJ/cm2 Develop in wafer track. Enter minimum resolution line: ______ um	

20	Plasma Etch Nitride, Trion Minilock (RF plasma) Use recipe: 50 mTorr, 50 sccm CHF3, 4 sccm O2, P=140W. Target time 11 minutes (660s) on 3/18/21 Etch through Nitride and Oxide on Poly Time/wafer = ____11min____ Verify nitride has been removed.	
21	10:1 BOE HF dip to remove oxide remnants. 1min.	
22	Strip Resist Use Solvent strip 5 + 5 min solvent clean + 5 min DI water rinse + SRD Min CD (target is 1µm)=____	
23	RCA Clean After first SRD, 1 min HF dip, Rinse, SRD to remove chemical oxide from SC2.	
24	CVC 601 sputter metal deposition of Al Thickness: 0.5µm (Target) 1200s gives .75 to 1 µm, so ~800s for target thickness. Hot/Cold Sputter Ar 20sccm Power: 2000W Pressure: 5mT Pre sputter: 300 seconds Standard Al sputter for 250 seconds Turn on heater per 601 manual instructions Set timer to 17 minutes temp 200C After 15 minutes set to hot sputter for 800 seconds Profilometry optional	
25	Photo Level 3: Metal Coat in SVG2 track. Recipe 4 no EBR. Expose using ASML Stepper Stepper job: PUCHADES_PRESS Energy: _______	

	Stepper mask: L3 “METAL” Develop in wafer track. CD-26 Recipe: Enter minimum resolution line: ______ um	
26	Aluminum etch wet - allow bath to sit for an hour before etch to achieve a uniform 40C throughout bath Etched with constant agitation for 4.5 minutes + 5 min DI water rinse on 3-22-21 Turn wafers 90º to allow bubbles to float up. SRD	
27	1 min Freckle etch Rinse (AlSi) + SRD	
28	Solvent strip resist	
29	Photo Level 4: Nitride (Inlet Holes for bulk Si etch) Coat in wafer track using AzMir resist. Soft bake 90C Recipe 4 no EBR Expose using ASML Stepper Stepper job: PUCHADES_PRESS Stepper mask: L4 “HOLES” Energy: 275mJ/cm2 Develop in wafer track. CD-26 Recipe: Default	
30	RIE Nitride Holes - Trion Minilock Etch through nitride & oxide and stop on bulk Si Time/wafer = ___15min____ Target: 15 min on 3-25-21 Verify nitride and oxide have been removed.	
31	Strip Resist Use Solvent strip 5 + 5 min solvent clean + 5 min DI water rinse + SRD Min CD (target is 1um)=____	
32	XeF2 Etch Bulk silicon (cavity) Recipe: Puch_IRD1 Time/cycle = 60sec XeF2 = 3 torr N2 = 2.2 Torr Run #__1___ No. of Cycles = 10 Run #__2___ No. of Cycles = 15	